SEA ICE AND ICE SHEET SURFACE ROUGHNESS CHARACTERIZATION AND ITS EFFECTS ON BI-DIRECTIONAL REFLECTANCE

A Thesis

by

YIRAN LI

Submitted to the Office of Graduate and Professional Studies of
Texas A&M University
in partial fulfillment of the requirements for the degree of

MASTER OF SCIENCE

Chair of Committee,	Andrew Klein
Committee Members,	Michael Bishop
	Sorin Popescu
Head of Department,	David Cairns

May 2018

Major Subject: Geography

ABSTRACT

The roughness of sea ice can affect its bidirectional reflectance distribution function (BRDF) thus influencing retrieval of its physical properties from satellite. We leverage WorldView-1 and Multi-angle Imaging SpectroRadiometer (MISR) remote sensing data sets collected over sea ice and the adjacent McMurdo Ice Shelf in proximity to McMurdo station to first characterize the roughness of sea ice and other snow surfaces and then examine the effects of surface roughness on satellites images of varying spatial resolutions. First, high resolution DEMs were created from stereographic WorldView-1 image pairs with NASA stereo imagery processing tool Ames Stereo Pipeline (ASP). A variety of geomorphometric measures of roughness, including roughness index, were characterized from the high resolution DEMs. Following adequate characterization of sea ice roughness, its impact on surface reflectance derived from optical satellites spanning a range of spatial resolutions was assessed.

ACKNOWLEDGEMENTS

I would like to thank my committee chair, Dr. Klein, for his instruction on my thesis research and help with every detailed problem I encountered during the work, and my committee members, Dr. Bishop, Dr. Popescu, for their guidance and support throughout the course of this research and inspirational courses they taught.

Thanks also go to my friends and colleagues and the department faculty and staff for making my time at Texas A&M University a great experience. I appreciate the great computing facilities and working environment offered by Department of Geography and College of Geoscience and a large amount of valuable satellite images provided by Carl Reim from Polar Geospatial Center.

Finally, thanks to my family members for their love and support.

CONTRIBUTORS AND FUNDING SOURCES

Contributors

This work was supervised by a thesis committee consisting of Dr. Klein and Dr. Bishop of the Department of Geography and Dr. Popescu of the Department of Ecosystem Science and Management. All the work conducted for the thesis was completed by the student.

Funding Sources

There are no outside funding contributions to acknowledge related to the research and compilation of this document.

TABLE OF CONTENTS

Page

LIST OF FIGURES

LIST OF TABLES

1. INTRODUCTION

Sea ice covers five percent to eight percent of the global oceans and is an important parameter in the global climate system and has significant influence on climate change. Different from sea ice, ice sheets are more constant, both in the morphology and motion. Ice sheets contain large amount of frozen water and cause rising sea level when they melt. Primarily located in polar areas, the monitoring and studying of sea ice and ice sheets are largely dependent on remote sensing technology.

These ice surfaces are rough and variable in their structure. A typical form of rough structure on ice surface is sastrugi. Sastrugi is decimeter-scale longitudinal ridges frequently formed by erosional process of katabatic winds (Herzfeld *et al.*, 2000). Surface roughness of ice has an influence on remote sensing results such as the spectral albedo which can be further used for retrieving the value of physical properties of ice and snow. The sunlight reflection pattern on the surface of ice can be examined by bidirectional reflectance distribution function (BRDF). Surface roughness was identified as an important factor that influence the BRDF firstly by Warren *et al.* (1998) and Leroux *et al.* (1998).

Sea ice and ice sheet roughness will be characterized from high resolution topographic data and impact on ice surface BRDF will be examined in this thesis. More specifically, this study will examine how the rough surface structures manifest themselves in optical satellite images such as MISR (Multi-angle Imaging SpectroRadiometer). In order to complete this research, rough ice surface structure will

be modeled and several metrics for characterizing the surface roughness will be examined. Furthermore, this research will quantify the relationship between the surface roughness and bi-directional reflectance of the sea ice and ice sheets measured from commonly used optical remote sensing satellites. This research will help understand what kind of and to what degree the impact of surface roughness would have on the radiation transmit process. The scale of the rough surface structure would also be of significance to the reflectance model. Thus, this study will be conducted on satellite images with a range of spatial resolutions and examine how surface roughness manifests itself across various spatial scales.

It was suggested by Herzfeld *et al.* (1999) that the information about the ice dynamical processes and its interaction with climate processes may be contained in spatial surface pattern of snow and ice. The research on the sea ice surface roughness provides opportunity to evaluate and quantify the surface structure of the sea ice that is crucial to BRDF and the derived Albedo of sea ice. If we lack of the information about the surface of sea ice, the retrieval of physical parameters would contain significant error which will further impede the estimating and monitoring of sea ice concentration, snow albedo, and subsequently the energy interaction between ocean and atmosphere and the influence of polar area on climate change.

How radiation transmit on the surface of sea ice and what kind of influence it would have on the image pixel value and further on the snow and ice property retrieval are of great significance to quantitative remote sensing. Failing to consider the surface roughness in the model for measuring snow albedo could result in retrieval errors

(Kuchiki *et al.*, 2011). The study on surface roughness can also help to classify the sea ice since the surface roughness varies with different type of sea ice (Nolin, 2007). Surface roughness is also one of the criteria to identify the stages of sea ice development in aging and melting process (Rivas *et al.*, 2006).

Two alternative research hypotheses are derived and listed below:

i. There is no measurable difference in the observed bi-directional reflectance of sea ice and ice sheets for areas with measured differences in surface roughness in the McMurdo Sound region of Antarctica.

ii. As the measured surface roughness increases, the influence of sastrugi and other roughness elements exhibit an increasing influence on the bi-directional reflectance of ice surfaces.

In order to test theses hypothesis, the following objectives must be accomplished:

i. Quantify surface roughness of sea ice and ice sheet surfaces in Antarctica near McMurdo station by using high resolution (2 meters or better) DEMs generated from satellite Imagery stereo pairs.

ii. Quantify the impact of surface roughness on the bi-directional reflectance of sea ice and ice sheets across multiple spatial scales. This multi-scale examination will include quantify surface roughness in various scales and compare with moderate resolution Multi-angle Imaging SpectroRadiometer (MISR). This will lead to a better understanding of how surface roughness variations manifest themselves in satellite images from a multi-scale perspective.

iii. Examine the specific effects of sastrugi (as identified in the DEMs) on the

measured bi-directional satellite reflectance.

2. LITERATURE REVIEW

2.1 Snow Surface Roughness and Angular Distribution of Reflectance

Polar sea ice is an important component of the global climate system and affects the earth's environment in many ways. It is one of the most reflective surface type on Earth. Thus spectral albedo and directional reflectance of snow and sea ice surface in polar area plays a significant role in the study of global climate and energy transfer (Zhou, 2003). The main source of energy for ice sheet ablation during summer comes from the absorption of solar radiation (Braithwaite, R. J., & Olesen, E. B., 1993). The surface albedo of snow and ice stands for the ratio of reflected radiation to incident solar radiation and is considered an important parameter in predicting ice sheet melting rate and the flow dynamics of outlet glaciers (Nolin and Payne, 2007). Surface roughness of the snow and ice allows the estimation of 3D structure of surface material and is important for surface classification in identifying snow and ice near retreating glaciers and at the boundaries of freezing or melting zone.

Because of the difficulty in collecting consistent snow reflection measurements, remote sensing with accessibility of visible and near-infrared wavelengths has becoming a desirable technique for monitoring snow physical parameters. A correction for Advanced Very High Resolution Radiometer (AVHRR) imagery was developed over sea ice by incorporating surface roughness and grain scale factors (Jin and Simpsin, 1999, 2000). Dozier and Painter claimed that incomprehension of several factors may introduce errors in remote sensing of snow properties which includes variation of

atmospheric conditions, impurities and snow wetness, grain radius, surface roughness, and vegetation canopy, etc. (Dozier *et al.*., 2004). Monitoring snow properties from space requires an accurate knowledge of its bidirectional reflectance factor (BRF) (Stroeve and Nolin, 2002; Stroeve *et al.*, 2005; Stamnes *et al.*, 2007; Scambos *et al.*, 2007; Painter *et al.*, 2009; Lyapustin *et al.*, 2009).

2.1.1 BRDF Models

The bidirectional reflection distribution function (BRDF) is defined as the ratio of radiance reflected into a particular direction (I_r, W m^{-2} sr^{-1} μm^{-1}) to the incident radiance (F_o, W m^{-2} μm^{-1}) in a particular direction by Nicodemus et al. 1977. A surface where BRDFs do not change with geometry of observation is termed a Lambertian surface. However, the observations in the past few decades demonstrated that the vast majority of Earth's surfaces are not Lambertian. An important property of Earth surface object, albedo, can be computed by integrating the BDRFs over the upper hemisphere.

Many BRDF models have been proposed by researchers since 1990. The number of parameters in these models varies from two or three parameters in simple models (e.g. Wanner *et al.*, 1995, martonchik *et al.,* 2002) to ten or more parameters in complex ones (e.g. Li and Strahler, 1992). The Rahman-Pinty-Verstraete (RPV) model calculates the bidirectional reflectance factor (BRF) of a surface as a function of the geometry of both illumination and observation (Rahman *et al.*, 1993). I It is a non-linear empirical model with three independent free parameters explaining the anisotropy of the surface. The RPV model is a three-parameter model based on a consideration of main aspects of BRDF shapes. The parameter accounting for hotspot effects is set to a fixed value in

some cases or forced to be equal to overall amplitude of reflectance level and noted as r_0; Parameter k is used to quantify the degree by which the observed bidirectional reflectance factors data represent the bowl or bell shape of the surface anisotropy; b controls the asymmetry of backward and forward scattering via a Henyey-Greenstein function in RPV model and replaced by an exponential scattering angle in modified Rahman-Pinty-Verstraete (mRPV) model (Liang, 2008).

The RPV model is useful in manifesting the structure of target feature since the anisotropy characteristic has relationship with the presence of shadows in complicated environments. The k parameter is derived from the Minneart function that describe the general shape of the angular distribution of reflectance: either increase with the illumination or observation zenith angle when $k < 1$ ("bowl shaped") or decrease with the illumination or observation zenith angle when $k > 1$ ("bell shaped") (Nolin, 2004). Therefore, k is frequently used to represent the degree of reflectance anisotropy by calculating the convexity or concavity of the bowl or bell shapes. Pinty *et al.* (2002) and Widlowski *et al.* (2001) have discovered that the anisotropic reflectance pattern is greatly affected by sub-pixel vegetation structure and density. They found that the presence of medium-to-high tree densities creates a bell-shaped angular signature, while homogeneous vegetation creates a bowl-shaped pattern on the bright soil substrate.

2.1.2 BRDF from Satellite Data

With the ability of the satellite sensors to acquire data in multiple bands and multiple viewing angle, more attention has been paid to multi-angle observations on the BRDF property at pixel scale. MODIS, Multi-angle Imaging Spectro-Radiometer

(MISR), Polarization and Directionality of the Earth's Reflectance (POLDER) are the most widely used remote sensing data for measuring BRDF. In particular, MISR is on board the NASA Earth Observing System (EOS) Terra satellite which was launched on December 18, 1999. MISR simultaneously measures the Earth in four spectral bands at nine widely spaced viewing angles (0, ±26.1, ±45.6, ±60.0, ±70.5) as illustrated in Figure 1. Derived geophysical products such as top-of-atmosphere (TOA) albedos, tropospheric aerosol optical depth, TOA and surface bidirectional reflectance factors (BRF), and other related parameters (Diner *et al.*, 1999) are publicly available.

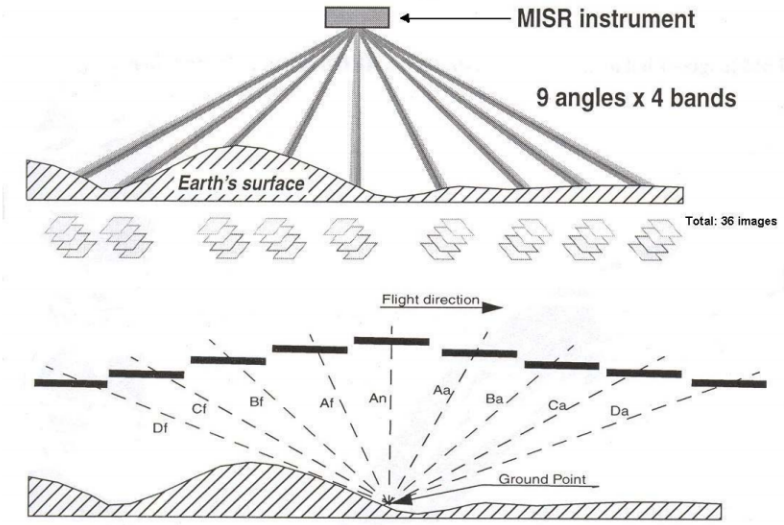

Figure 1 MISR on the EOS-Terra satellite views land surface at nine angles: 26.1 (A), 45.6 (B), 60 (C), 70.5 (D) in forward (f) and afterward (a) directions. All nine cameras view a single location within approximately seven minutes (reprinted from Diner et al., 1999)

Chen et al. (2009) compared MISR and MODIS BRDF products at four land cover types and discovered that both BRDF models have better representation on directional reflectance at some viewing angles, and representation of both BRDF

products tend to be impaired with an increase viewing zenith angle. Wu et al. demonstrated that the BRDF model parameters derived from MISR multi-angle reflectance data are useful in vegetation mapping. Wu et al (2011). explores snow BRDF over snow covered regions using MODIS and MISR surface reflectance products by utilizing linear Ross-Li model and nonlinear modified Rahman model respectively (Wu *et al.*, 2011). They discovered that the angular distribution of reflectance in different bands are similar and the minimum reflectance occurs in the nadir region and its extension in backward direction.

2.1.3 BRDF from *in situ* Measurements

The ability of satellites to provide multi-angular observations at regional or global scale can be restricted by a satellite orbit and by its sampling capability (Zhang et al., 2015). Therefore, field experiments covering sufficient angular observations have been conducted to estimate anisotropic reflectance for decades. Initially, the snow BRDF was simulated by using radiative transfer equation (RTF) in a horizontally homogeneous model (Wiscombe and Warren, 1980). However, the measured bidirectional reflectance can markedly differ from model results obtained with the assumption of a flat snow surface (Painter and Dozier, 2004). The calculation of snow BRDF is suggested to include the roughness of the snow surface to improve the agreement between theoretical and experimental results. The alteration of snow BRDF caused by presence of surface roughness can be a possible cause of error for remote sensing of snow parameters (Kuchiki *et al.*, 2011).

The influence of snow roughness on bidirectional reflectance has been

investigated in several researches.Kuhn (1974) noted that the shading influence of the sastrugi introduces a daily variation if albedo of about two percent (Kuhn, 1974). By measuring anisotropy reflectance from a 22 m tower at South Pole (Warren et al., 1998). Warren et al. (1998) demonstrated that sastrugi can alter the reflectance pattern significantly relative to a flat surface, particularly at large viewing angles and especially in the forward scattering direction with measuring normalized BRDF, or "anisotropic reflectance factor" R They proposed two reasons that sastrugi alter albedo andthey recommend near-nadir views for accurate remote sensing over snow when inferring properties of the surface or planetary albedo. Leroux and Fily (1998) found that the sastrugi in their model caused the albedo at 900 nanometers to drop from 0.90 for a flat surface to 0.85 when sastrugi is parallel to the solar incident direction or 0.81 when sastrugi is perpendicular to solar incident direction. They also discovered a dependence of the directional reflectance on the orientation of rough surface features. Zhuravleva et al. (2011) examined sastrugi effects on snow-reflected solar radiation with a statistical approach and discovered that neglecting snow surface roughness in the SRF (snow reflection function) calculations may bias snow grain size retrievals Kuchiki et al. (2011) accessed variation of snow grain size (typically 50-1000 □□) retrieved from MODIS by assuming a flat snow surface and the result implies that the assumption caused a retrieval error up to several hundred micrometers at band2 (0.86 μm) and a few tens of micrometers in band 6 (1.64 μm).

Surface roughness is also known for its significantly impact on microwave emission of the sea ice/snow surface in estimating sea ice concentration and extent

(Sungwook, 2009). Hong developed a method to estimate the small-scale roughness of sea ice using the polarized reflectivity from characteristics of the incident angle of AMSR-E data (Hong, 2010). Stroeve demonstrated that small scale roughness (i.e., millimeter to meter scale) significantly impact the observed Polarimeric Scanning Radiometer (PSR) brightness temperatures (Tbs) and polarization ratios (PRs) decreases as the surface become more ridged (Stroeve *et al.*, 2006). They proved that knowledge of surface roughness can improve snow depth and sea ice concentration retrievals from passive microwave Tbs.

2.1.4 Normalized Difference Angular Index (NDAI)

NDAI was first proposed by Nolin *et al.* (2002) to characterize angular scattering of snow and ice surface. The index was applied to MISR atmospherically corrected bi-directional reflectance (for top-of-atmosphere) or hemispherical-directional reflectance (for surface quantities) measured from corresponding forward and backward camera. The forward scattering indicates generally smooth surfaces while backward scattering suggests rough surface. Therefore, a positive value of NDAI indicate backward scattering exceeds forward scattering and the surface is relatively rougher.

The research conducted by Nolin et al. (2007) suggested that NDAI images along with the NIR albedo images has significant potential to improve unsupervised classification of ice sheet surface type. By comparing the NDAI with the pre-computed airborne LiDAR-derived surface roughness data, they also demonstrated the existence of strong correlation with $r = 0.89$ when LiDAR traversing the glacier from east to west. Shi *et al.* utilized NDAI as one of three features in classification algorithms to detect

clouds and in polar regions. NDAI is selected to differentiate cloud and clear region because cloudy area tends to be much brighter than clear area in forward scattering direction (2004).

2.2 Surface Roughness Characterization

Surface roughness discussed in this study is defined as the topographic expression of surface at horizontal scales of centimeters to a few meters. The most representative surface structure that we are interested in is sastrugi. There is no standard method for quantitatively characterizing sea ice surface roughness, and the snow and ice surface roughness has been characterized and examined in many experiments with a variety of measurement techniques. The selection of the roughness metrics applied in the research depend on purpose of the experiments. Kuchiki *et al.* measured bidirectional reflectance for rough surface artificially produced with sastrugi-like linear ridges in 2009. The surface roughness with sastrugi is characterized by the H (height of ridge)/W (width of ridge) and relative sastrugi azimuth angle from the solar azimuth.

For large scale sea ice roughness, airborne and space-borne methods are preferred comparing to field measurement. Terrestrial light detection and ranging (LiDAR) is one of the technologies that commonly used in measuring and understanding sea ice surface topography. Landy *et al.* developed a numerical model with LiDAR observations to measure the centimeter scale surface roughness of sea ice (Landy *et al.*, 2015a). The surface roughness is characterized by root-mean-square (RMS) roughness height, correlation length, and autocorrelation function. Most of the surface roughness measurements using terrestrial laser scanning system are based on 1-D profile analysis.

The 1-D measurements are not stationary when roughness vary a lot between adjacent profiles or large sampling interval and sample length exist (Landy *et al.*, 2015b). Thus 2-D measurements of surface roughness is considered to be more precise than the 1-D profile-based analysis.

A variety of roughness metrics developed to evaluating roughness of a surface are based on autocorrelation analysis. Fassnacht mentioned three common sets of roughness metrics: random roughness (RR), auto-correlation (AC), and variogram analysis (Fassnacht *et al.*, 2015). The random roughness is calculated as the standard deviation of the elevations from the detrended surface (mean surface). The random roughness doesn't take into account the spatial structure of roughness but the effect on detrended surface. The auto-correlation also use the detrended surface data and and is calculated as correlation coefficient of each sample along the surface with respect to the previous sample on a regular interval. Variogram analysis considers the spatial structure of the surface and has no requirement for continuous dataset or regular interval data. The elevation variance between each pair of locations is calculated as a function of the distance between points.

Many metrics for characterizing surface roughness in terms of the variability of elevation values in DEM have also been proposed to quantify spatial variability of morphometric parameters over a particular scale. Terrain analysis can be easily performed in a GIS environment by converting the DTM to a raster grid. For example, Weiss presented Topographic Position Index (TPI) to characterize watersheds in 2001. TPI compares the elevation of each cell in a DEM to the mean elevation of a

neighborhood with any reasonable shape. Melton proposed a Melton Ruggedness Number (MRN) to model flow accumulation related index. The index is calculated as the ratio of difference between maximum and minimum elevation and square root of basin area size (Melton, 1965). Riley et al. developed Terrain Ruggedness Index (TRI) calculated as difference between the value of a DEM cell and the mean of surrounding cell in a neighborhood window (Riley *et al.*, 1999). Nolin et al. examined the surface roughness of western Greenland by calculating the root mean squared deviation of the surface from a best fitting plane (Nolin *et al.*, 2007). She also demonstrated that MISR (multi-angle imaging SpectroRadiometer) data can be used as a proxy to characterize roughness of sea ice and ice sheets over Greenland and Antarctica by calculating a normalized difference angular index (NDAI). Grohmann *et al.* derived the surface roughness from absolute standard deviation of all values within a window and as the deviation from a best fit plane (Grohmann *et al.*, 2009). Trevisani and Rocca developed a multi-scale and directional image texture analysis operator (MAD) to offer a robust description of surface texture, including surface roughness (Trevisani *et al.*, 2015). MAD takes residual DTM calculated as subtracting the smoothed DTM from the original DTM as input.

2.3 DEM Generation From High Spatial Resolution Satellite Images

More and more space-borne optical remote sensing satellite sensor are capable of producing high spatial and radiometric resolution stereoscopic images pairs. Comparing with time-consuming traditional terrestrial surveying methods and GPS techniques, satellite images provide wide (> 10 km) swath widths and frequent repeats (Noh *et al.*,

2017). What's more, the ability of accessing data in remote and impassable place makes it the best choice for DEM generation in polar area. Different algorithms of extracting DEM from those very high resolution (VHR) images have been developed alongside the satellite improvements.

The workflow for DEM generation from stereoscopic images can be summarized as follow steps (Shin *et al.*, 2003):

- Feature selection in one of the stereo-pair
- Identification of the conjugate feature in the other scene
- Intersection procedure
- Point densification

A fully-automated DEM extraction algorithm named Surface Extraction with TIN-based Search-space Minimization (SETSM) for processing large numbers of stereo pairs is developed by Noh (2015). Their algorithm only requires sensor model information along with the satellite image and has no need of other *priori* knowledge for the target. NASA also provided an automated, open source software Ames Stereo Pipeline (ASP) to help people generating DEM from very-high-resolution (VHR) commercial imagery of the Earth. Shean *et al.* outlined a processing workflow for DigitalGlobe WordView-1 and WorldView-2 stereo image. They evaluated ASP correlator options, benchmark test results and two case studies of DEM accuracy.

2.4 Accuracy Assessment of Generated DEM

A lot of studies has been carried out to evaluate the accuracy of resulting DEM from VHR optical remote sensing stereo image pairs. Evans et al. assessed the accuracy

of DEM generation from Cartosat-1 data with three different DEM derived from National Elevation Dataset (NED), ASTER, and ARTM (Evans *et al.*, 2008) by using PCI software and ENVI DEM module. The results indicate approximately 5 m horizontal accuracy and average 4 m vertical accuracy. Buyuksalih et al. reached a vertical accuracy of 3.2 m corresponding to an x-parallax of 0.33 pixels in DEM generation with automatic image matching method by checking against a reference DEM from topographic maps 1:25000 (Buyuksalih *et al.*, 2004).

3. METHODOLOGY

3.1 Study Area and Satellite Dataset

Scientists divide the Antarctic ice pack into five sectors for better study of sea ice patterns and trends: The Weddell sea, the Indian Ocean, the western Pacific Ocean, the Ross Sea and the Bellingshausen and Amundsen seas. Antarctic sea ice extent typically reaches its maximum in September and minimum in February. This study investigates sea ice in the Ross Sea which is one of the three main sources of Antarctic Bottom Water, a major component of the global ocean circulation system (Johnson, 2008). Because of this and proximity to McMurdo Station, the logistical hub of United States Antarctic Science, many studies has been done conducted to understand the underlying physical mechanisms of sea ice including by remote sensing. This work attempts to contribute to our understanding of sea ice, and to a lesser extent ice shelf reflectance in the Ross Sea as manifests itself in multiple satellite images.

The satellite dataset used to derive high resolution DEM is Digital Globe WorldView 1. After the DEM was generated, several remote sensing datasets from MISR were selected that cover the area of the DEM.

In order to avoid the computational difficulty on per pixel analysis and model application over the entire image, several representative locations are selected to investigate reflectance based on the roughness map and local understanding of sea ice and the McMurdo ice shelf. A description of the generation of the roughness map and the criteria for the selection of specific locations will be elaborated in the following sections.

3.1.1 MISR Specification and Processing with MISRToolkit

The Multi-Angle Imaging Spectroradiometer (MISR) is one of the sensors flown aboard the NASA's Earth Observing System (EOS) Terra satellite. MISR has nine cameras pointed at 9 fixed discrete angles. One nadir and four viewing angles in both forward (f) and afterward (a) direction along the track of satellite. It provides a series of geophysical products by simultaneously viewing the Earth in four wavelengths (446, 558, 672, and 866 nm) at nine angles (0°, ±26.1°, ±45.6°, ±60.0°, ±70.5°). The MISR sensor has high radiometric resolution and a wide dynamic range which is desirable for snow-covered surface detection. MISR data is distributed in HDF-EOS data format and use Space Oblique Mercator (SOM) projection with a spatial sampling of 257 meters in the red bands and nadir bands, and 1100 meters in all the other bands. Globally, there are 233 distinct but overlapping MISR paths that comprise one scan of the entire Earth. Data are collected by the MISR sensors from the 223 paths repeatedly in every 16 days. The revisit time for a particular location under a variety of angular conditions is about 9 days at the equator and 2 days at polar areas. The Terra platform that carries MISR revolves once around the planet in 98.88 minutes and each complete revolution is called an orbit. The orbit number increases by 1 after each orbit and was labeled as 1 at launch. Therefore, while a path number can determine the geographic location of MISR products an orbit number is required for knowing the acquisition date of an image along a certain path (Tao Shi and Bin Yu, 2004).

Because of our focus on the surface angular signature, it is critical to have a precise understanding of how the solar zenith and azimuth are defined in MISR data.

Different from the conventional definition in some radiative transfer models, solar azimuth angles measured by MISR instruments are measured clockwise from the local north to the direction pointing away from the Sun, rather than toward it. So MISR a sun azimuth is 0° when the sun is due south of the ground point. Figure 2 indicates the solar illumination geometry in MISR imagery acquisition.

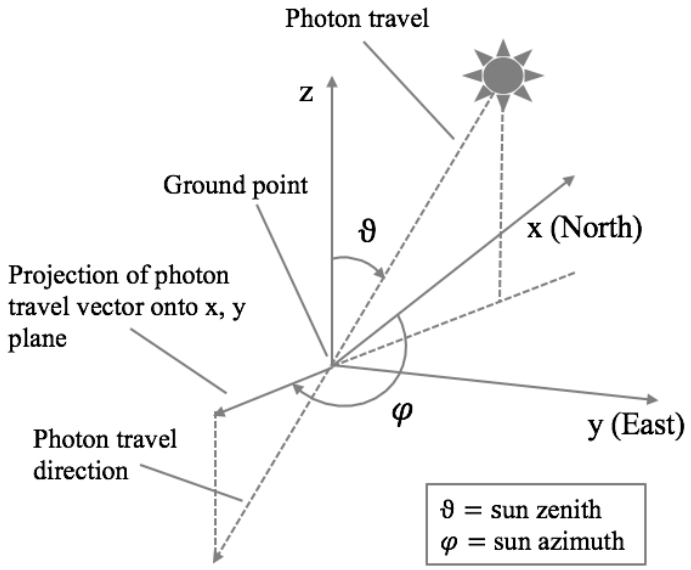

Figure 2 Sun angles defined in MISR

This study used MISR path 59 data acquired on 29 December 2013 from block 154 on orbit 074640. Three specific MISR data products were used: 1) the MISR Level-1B2 Ellipsoid-projected Radiance product (MI1B2E); 2) the MISR Level-1B2 Geometric Parameters product (MI1B2GEOP); and 3) the MISR Level-2 Land Surface product (MIL2ASLS). MI1B2E contains TOA (top-of-atmosphere) radiances that are calibrated, geometric corrected, and projected to a Space Oblique Mercator grid. The MI1B2GEOP dataset provides information about the solar and view geometry and

geolocation information in data acquisition at 17,600 m spatial resolution. Three model parameters (r_0, k and b; a.k.a. BRFModParam1, BRFModParam2, and BRFModParam3) required for the modified RPV (MRPV) model (Diner *et al.*, 2008) and the measure of the fit residual (Δ) are directly archived in the Level 2 land surface product for all available wavelengths. Figure 3 illustrates the solar position at the time of each MISR acquisition and the geometry of its nine sensors. The forward-pointing sensors and the nadir sensor are marked in red and aft pointing sensors are marked in blue. The flight direction is runs in a direction from the forward-pointing sensors to the aft-pointing sensors. As we can tell from Figure 3, path 59 is descending path over Antarctica. Considering the sun position along with the sensor direction, the forward viewing cameras measure backward scattering and the afterward cameras are measuring the forward scattering.

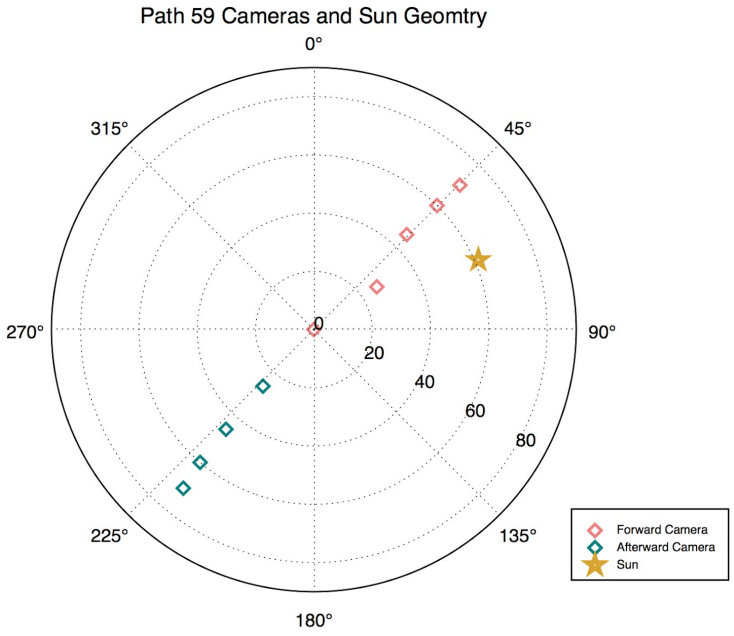

Figure 3 Forward (Df, Cf, Bf, Af, An) cameras (red) and Backward (Aa, Ba, Ca, Da) Cameras (blue) (i.e. data acquisition) and sun geometry in MISR path 59, orbit

074640, block 154. All the angles are average value calculated from MISR Level-1B2 Geometric Parameters product

Because of the original MISR datasets are distributed in HDF-EOS stacked-block grid format and in the Space Oblique Mercator (SOM) map projection, specialized tools are required to access and process them. The MISR Toolkit (MTK) is a programming interface to the Python programming language to access and manipulate MISR Level1B2, Level2, and ancillary data products. MISR data products are accessed in an HDF file structure of file containing grid (band), field (Radiance, RDQI, DN, Equivalent Reflectance), region (region defined by path and block number), and data planes (*numpy* array). MTK Python bindings were used to read MISR images based on geographic extent of the study area as *numpy* arrays. Further processing was conducted based on the resulting *numpy* arrays. MTK also provided a crucial function to perform coordinate conversions between latitude/longitude and SOM x/y, block/line/sample in grid.

3.2 DEM Generation from WordView1

A Digital Elevation Model (DEM) is one of the fundamental components of the terrain analysis. Besides the traditional surveying methods, very high resolution (VHR) remote sensing images acquired in stereo pairs have become popular in DEM generation. Since a DEM is the primary input in the following surface roughness index calculation, it is critical to produce reliable high resolution DEMs over our study area.

3.2.1 WorldView Stereo Imagery

Digital Globe's WorldView 1 stereo image products with 2-meter spatial

resolution are ideal for users to generate VHR DEMs. These products are orthorectified in the GeoTIFF format and are ready to use as the input for DEM generation procedures.

This research utilizes WorldView 1 Level 1B satellite images and the corresponding XML file which contains both the exact linear camera information (named as *dg* in ASP) and its RPC approximation (named as *rpc* in ASP). The WorldView1 images used in this research were provided by the Polar Geospatial Center and figure 4 shows the images and where they are located relative to McMurdo station and Ross island.

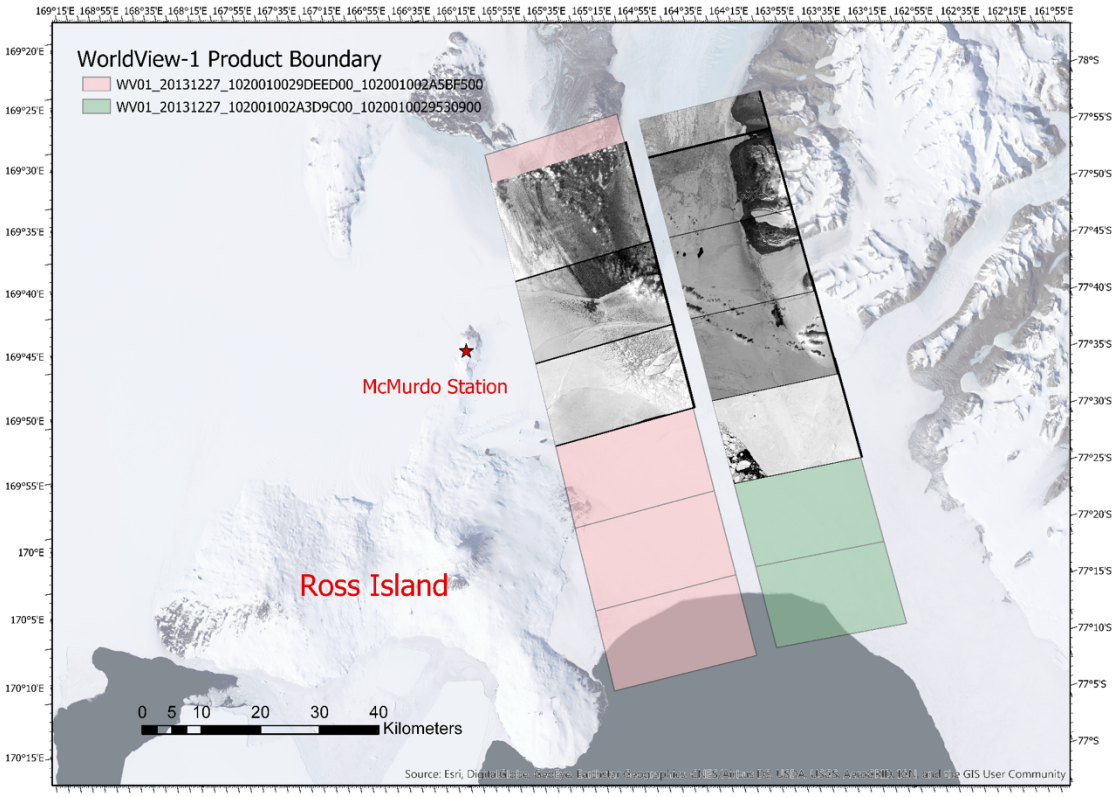

Figure 4 Subsets of two WorldView1 products

3.2.2 NASA Ames Stereo Pipeline

The Ames Stereo Pipeline (ASP) is an open source 3D surface construction and visualization command-line program developed by the Intelligent Robotics Group (IRG) at the NASA Ames Research Center. At first, it was designed to process non-terrestrial imagery, but it is now being widely used to process Earth imagery from commercial providers that provide RPC camera models for their products. There are four key steps in the DEM generation procedures, 1) handling CCD boundary artifacts, 2) map-projecting the images, 3) stereo correlation, 4) point cloud alignment, 5) converting point cloud to DEM.

In order to avoid the discontinuities in the DEM resulted from subpixel artifacts in WordView images during DEM generation, a tool called *wv_correct* was utilized. Then the corrected images along with the low-resolution reference DEM are used as input for *mapproject* tool prior to *stereo*. The reference DEM selected was the Radarsat Antarctic Mapping Project Digital Elevation Model, Version 2 (RAMPv2) with pixel size of 200 m in binary grid format referenced to WGS84 datum ellipsoid. As a pre-processing step, the objective of map projecting is to roughly align the stereo pair by mapping left and right images onto the low-resolution smooth terrain. In this case, we used RPC approximation (*-t rpc*) camera model which is accurate enough while being much faster than an exact linear camera model.

Stereo correlation is the core function of ASP and it works by matching a neighborhood of each pixel in the left image to a similar neighborhood in the right one. Because of the cloud noise in our WorldView images, the pixels covered with cloud were missing in the output DEM. The parameter *corr-kernel* was set to be 15 as it

determines the size (in pixels) of the correlation kernel. Increasing the kernel size helps fill in regions where no match point was found but requires longer processing time. After the disparity map was initialized, every pixel will have either an estimated disparity value or be marked as invalid. All the valid pixels are then adjusted by a Bayes EM weighted affine adaptive window correlator which we set as *subpixel-mode* to 2. This method produces very high quality stereo matches with limited image noise.

The *point2dem* program produces a DEM from the point cloud file derived from *stereo* step. The resulting DEM file is in GeoTIFF format with georeferencing information and the projection is manually set to be EPSG 3031 Antarctic Polar Stereographic. No data pixels are set to -9999.0 and *dem-hole-fill-len* is set to 50, so the holes less than 50 m on the output DEM are filled.

Due to the very high resolution of WorldView 1 images and the resulting large data size (about 500 MB for one subset of a product), as well as the complexity of the stereo pipeline algorithms, it takes a large amount of CPU computational power and considerable time to process even a small image. For example, a pair of stereo images with size of 991.8 MB and 845.2 MB respectively, took 12 hours to process on a MacOS operation system with 2.7 GHz processor and 8 GB memory. To complete the task more efficiently, ASP was run on a Linux virtual machine provided by with an allocation of 8 virtual CPUs and 16 GB memory.

3.3 DEM Registration

Because of the inherent inaccuracies originating from the original data that were used to generate the DEM and errors in the DEM generation process, the point cloud

derived from WV1 stereo pairs was aligned point cloud data from a different source to diminish the potential biases by *pc_align* program.

The LiDAR data used in this study was downloaded from Operation IceBridge Data Portal with the spatial searching box same as the boundary of the DEM and temporal filter is set to a range less than 30 days to the date of WorldView images used in DEM creation was acquired (December 27, 2013). Eventually, 11 tracks with 22 files are qualified for further study. All the LiDAR data are IceBridge ATM L1B Elevation and Return Strength Version 2 with the dataset ID of ILATM1B. Every LiDAR data file is in hdf5 format and has an associated xml file providing metadata containing ancillary information, such as sensor name, date of survey and spatial coverage. The average point density of ATM LiDAR dataset used in this study is one laser shot per 10 m^2. The information required for DEM registration were latitude, longitude, and elevation. The elevation is referenced to the WGS84 ellipsoid (ellipsoid height). A python script was written to automatically loop through all relevant IceBridge files, extract longitude, latitude, and elevation and write this information to new comma separated value (csv) files as three fields. This information was used as a more accurately positioned (~0.1-0.2 m vertical accuracy) elevation source for the DEM generated from World View 1. The input other than latitude, longitude, and elevation that required by *pc_align* program is a priori guess for the maximum displacement expected in the alignment process, i.e. the maximum distance those points are allowed to move. This parameter is set to 500 in this study. Figure 5 illustrated the track of LiDAR dataset and the DEM converted from it.

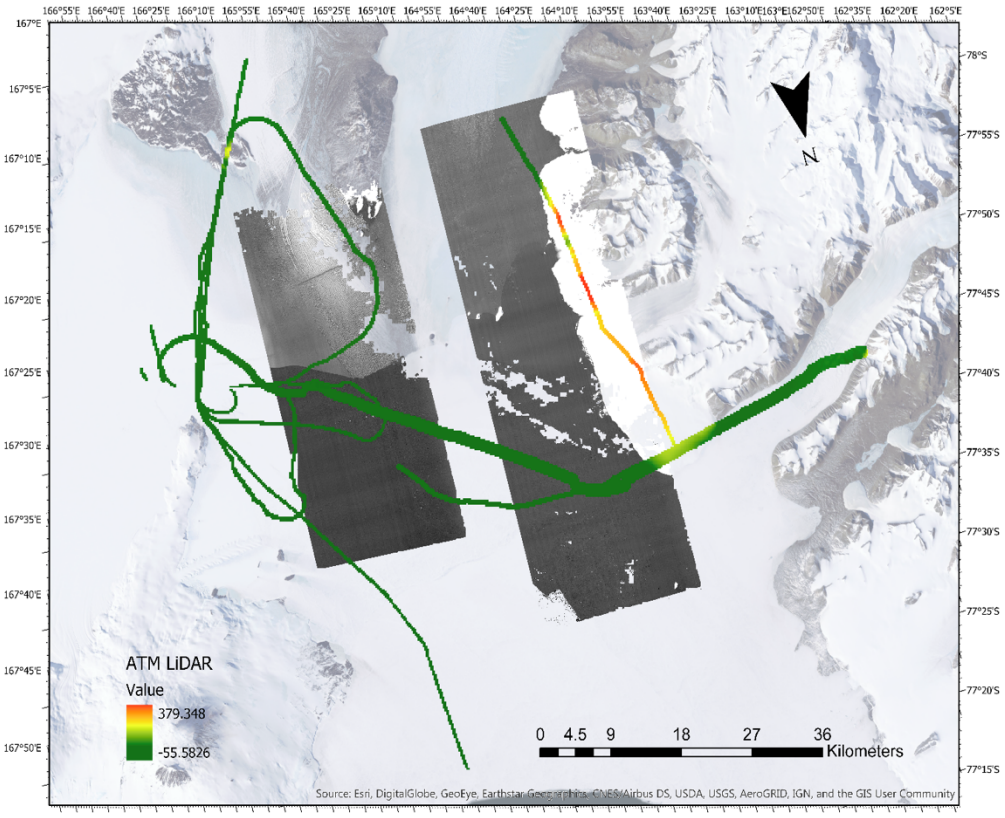

Figure 5 ATM LiDAR dataset selection (pink) over the study site

3.4 Surface Roughness Characterization

As discussed by Smith (2014), varying metrics exist for characterizing surface roughness. In this study the TRI (Terrain Ruggedness Index) is computed as the mean of the absolute differences between the value of a cell and its neighboring cells by summing the squared difference in elevation between a center grid cell and its neighboring cells, and then taking the square root of the sum. The computation strategy of TRI is illustrated in figure 6. This index was first proposed by Riley and others (Riley *et al.* 1999) to quantify topographic heterogeneity. Before that, most researchers describe terrain mainly in qualitative terms which is undesirable for more complex scientific

analysis. TRI was adopted in this study because it merely relies on DEM and relatively easy to understand and calculate. As a pixel-based index, it is also very flexible at detecting roughness at various spatial scales and different directions. Normally the surface roughness should be calibrated to contain the ice surface height only to remove the effect of longer-wavelength variations in terrain. However, as the study area of interest is mainly covered by sea ice and ice shelf, it is reasonable to extract surface roughness directly from DEM elevations.

TRI index was applied to DEM we generated from WorldView 1 stereo image pairs by running a series of Python scripts. DEM in GeoTiff raster format was read in as 2D *numpy* array by functions provided by GDAL (Geospatial Data Abstraction Library). The geographic transformation information including x and y coordinate of upper left corner of the upper left pixel, pixel width and pixel width (equal to pixel width since DEM pixel is square) were stored in variables and was assigned to the resulting array from TRI index calculation. The weight for each surrounding pixel in non-directional TRI is set to 1. Four directional TRI indexes were also computed by changing the weight of cells in corresponding direction and the weight matrixes are illustrated in figure 7. The cell size in denominator of the function serves for the purpose of normalization and comparability between various spatial scales.

-1,-1	0,-1	1.-1
-1,0	0,0	1,0
-1,1	0,1	1,1

If each square represents a grid cell
On a digital elevation model, then TRI
= $[\sum(x_{ij} - x_{00})^2]^{1/2}$/CellSize, where x_{ij}
= elevation of each neighbor cell to cell x_{00}

Figure 6 Cell location coding and TRI calculation function

1	1	1	4	0	0	0	4	0
1	0	1	0	0	0	0	0	0
1	1	1	0	0	4	0	4	0

Weight matrixes
(1) directionless,
(2) Northwest- Southeast,
(3) North-South,
(4) Northeast-Southwest,
(5) East-west (from left to right, top to bottom)

0	0	4	0	0	0
0	0	0	4	0	4
4	0	0	0	0	0

Figure 7 Weight matrixes in TRI index computation

3.4.1 Scale Effects

The window size of the statistical unit (moving window) is very important. According to previous research, some principles must be followed. The optimum window size should match the scale of surface structure of concern to keep its integrity and be adaptable to any variation form in our study site (Zhou *et al.*, 2008).

To evaluate appropriate scale of representing roughness on Antarctic sea ice, the selected surface roughness metrics were applied on DEMs with increasing moving-windows sizes of 3x3, 5x5, 7x7, 9x9, 11x11, 13x13, 15x15, 17x17, and 27x27 increasing up to 117x117. With the window size increases, the statistics changed rapidly at the beginning where the window size was on the spatial scale of sastrugi and other roughness elements on the sea ice and ice shelf.

3.5 Snow BRF from MISR

Remote sensing of land material and atmospheric aerosol, cloud, and trace gases in cryosphere from satellites relies on thorough knowledge of the snow angular reflectance (Kokhanovsky *et al.*, 2012). Typically, the snow exhibits a directional scattering signature that is very different from other land surface because of its maximum reflectance in forward scattering (Arnold *et al.*, 2002).

To examine the influence of sea ice and ice sheet roughness on snow angular reflectance, multi-angle remote sensing observation data from the Multi-Angle Imaging SpectroRadiometer (MISR) was utilized.

While the widely used Ross-Li model is designed to simulate the radiance transfer of the vegetation canopy, it is not ideal for capturing snow's BRDF features because of strictly defined coefficients. Therefore, the Rahman-Pinty-Verstraete (RPV) model model was used to study the BRDF of snow on sea ice and an ice shelf over the study region. In contrast to kernel driven models, the RPV model is a semi-empirical model with three parameters (RPV3P) or four parameters (RPV4P). The RPV4P model has improved ability to model bidirectional reflectance when hotspot effects (a peak in

reflected radiation from a target in the retro-illumination direction) are prominent (Koukal et al., 2010). The PRV model adopted by MISR data product can be described by the following equation (Diner et al., 1999, Rahman et al., 1993):

$$R_{model} = \left(r_0 \times \frac{cos\theta^{k-1} cos\vartheta^{k-1}}{(cos\theta + cos\vartheta)^{1-k}}\right) \times \exp[b \times p(\Omega)] \times h(\theta, \vartheta, \emptyset) \quad (1)$$

In equation (1), r_0, k, b are three free parameters. θ and ϑ represent the observation zenith angle and solar illumination zenith angle. $\emptyset$ is the relative azimuth angle between the solar and the sensor. $\emptyset$ is equal to zero when the illumination source is behind the observing sensor. Because how solar azimuth angle is provided in MISR follows a different rule to some other radiative transfer models, $\emptyset$ is calculated as the difference between solar azimuth angle having 180º deducted and camera azimuth angle. The function $p(\Omega)$ is assumed to depend on scattering angle Ω only which is the angle between the incident and reflected radiance directions. It can be calculated as the function of θ, ϑ and $\emptyset$：

$$p(\Omega) = \cos\Omega = cos\theta cos\vartheta + sin\theta sin\vartheta cos\phi \quad (2)$$

The function h is a parameter to describe the hot spot:

$$h(\theta, \vartheta, \emptyset) = 1 + \frac{1 - r_0}{1 + G(\theta, \vartheta, \emptyset)} \quad (3)$$

$$G(\theta, \vartheta, \emptyset) = [tan\theta^2 + tan\vartheta^2 + 2(tan\theta tan\vartheta) cos\emptyset]^{1/2} \quad (4)$$

R_0 describes the overall amplitude of reflectance level; k is used to quantify the degree by which the observed bidirectional reflectance factors data represent the bowl or bell shape of the surface anisotropy; b accounts for the predominance of backward and forward scattering.

Three model parameters (r_0, k, b) values are available from MISR standard level 2 land surface product. Three parameters are used in forward mode in the angular function of MRPV model to calculate the reflectance of any view angle (θ, ϑ, $\emptyset$). The definition of the angular geometry of illumination and observation used in BRDF model are defined is illustrated in figure 8.

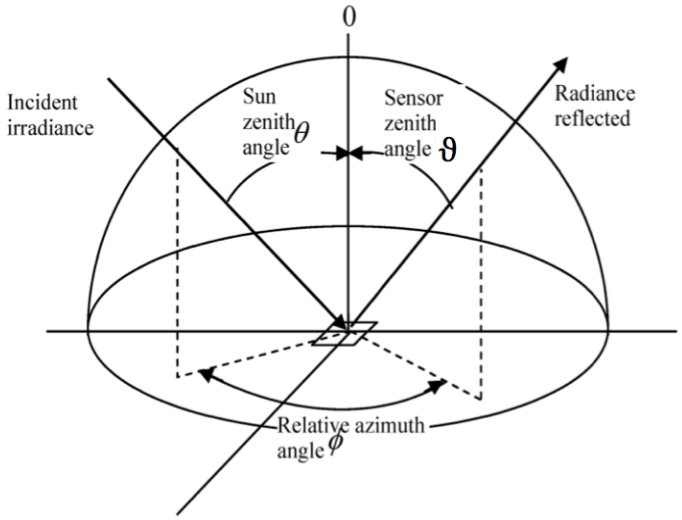

Figure 8 Geometry of illumination and observation

This study examined k parameter and the MRPV model derived from it with other parameters over the rough sea ice/ice shelf areas and investigated the effects of surface roughness on the angular signature of snow and ice on sea ice and the McMurdo Ice Shelf. For each MISR waveband, pixels were selected and compared with TRI surface toughness map to examine possible relationships between the MISR angular measurements and surface roughness.

3.6 Feature Selection

One of the main objectives of this research is to identify the difference in the pattern of anisotropic reflectance over snow and ice surfaces of varying roughness. The angular reflectance of a pixel relies on both the intrinsic anisotropic scattering pattern of the components in that pixel and the arrangement of those components in three-dimensional structure (Nolin, 2002).

Thanks to the innovative multi-angle remote sensing instruments like MISR angular reflectance information of the remote locations can be examined on a large scale. According to the spectral signature of snow and ice, the four bands provided by MISR (Red, Blue, Green, NIR) have similar characteristics. In the visible and near infrared wavelengths, new snow typically has an albedo (reflected solar radiation/ incoming solar radiation) around 90%. Old snow or multi-year snow that are aged and contain accumulated dust can have albedo as low as 40% (Foster et al., 1987). In this study, the red band was selected to investigate snow and ice angular signature as the red band radiances have the highest spatial resolution (275 m) in all the observation angles. The radiance acquired from the eight off-nadir angles and nadir angle cameras on MISR were plotted. From these two features that are able to capture the characteristics of radiance variations manifested in the plot were determined in the following section, the rationale of why these features were selected and how NDAIs capturing these features were computed are explained.

Multiple sites are selected with a prior knowledge to represent representative surface types in our study area on sea ice and ice shelf with snow or snow free, and one

glacier. The geographic locations of those sites are indicated in the figure 10 and detailed information about those sites are listed in the Table 1.

3.6.1 Normalized Differential Angular Index (NDAI)

Most of the remote sensing experiments measure the spectral information to infer physical properties of Earth surface and atmosphere. However, unique angular scattering information of the sea ice and ice sheet surface can be acquired from multi-angle satellite images. Normalized Differential Angular Index (NDAI) was used as a proxy for glacier surface roughness calculated as combination of forward and backward radiation scattering (Nolin *et al.*, 2002). The normalization effectively eliminates the atmospheric influence and isolates the contribution of the directional impact of each band. Considering Sun azimuth angle during daylight in Antarctica area, forward scattering is recorded by afterward pointing cameras and the backward scattering is measured from forward cameras. Positive NDAI value indicate the dominance of backward scattering and by inference relatively rougher surfaces while negative values suggest that forward scattering is greater than forward scattering corresponding to a smooth surface conditions.

$$\mathrm{NDAI} = \frac{\rho \mathrm{Df} - \rho An}{\rho Da + \rho \mathrm{An}} \qquad (5)$$

The dataset used for computing NDAI was MISR Level-1B2 Ellipsoid-projected top-of-atmosphere unscaled radiance data. All the satellite datasets was georeferenced and atmospherically corrected.

3.6.2 Band Ratios

To provide a more straightforward conception of how radiance varies over changing camera viewing angle, the radiance value obtained from MISRs nine cameras over eleven sites are plotted together on the same graph (figure 9) and organized by 4 MISR spectral bands. The positive zenith angles stand for forward cameras and negative values are for backward cameras.

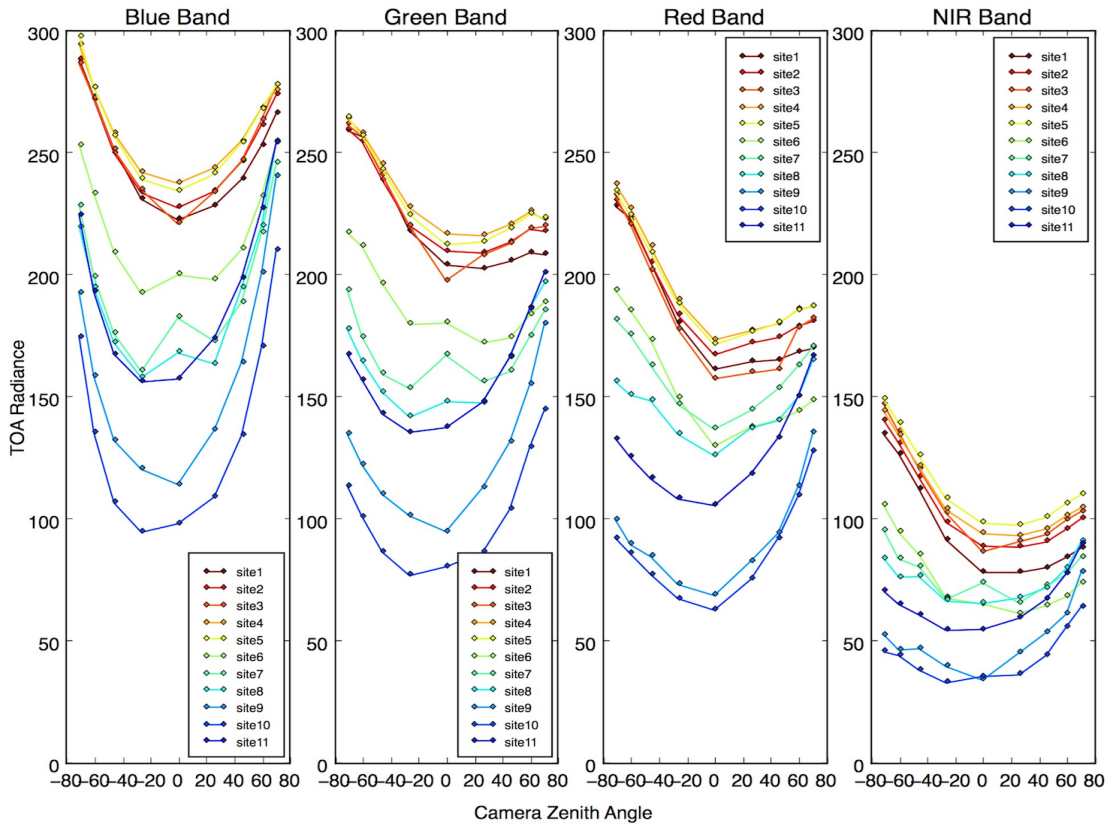

Figure 9 MISR Radiance value in nine viewing angles from site 1 to site 11

As can be seen from the figure 9, radiances decrease as the wavelength increases which is consistent with the known spectral properties of snow and ice. The radiance varies greatly by the camera observing zenith angles. The shape of the radiance curve indicates strongly antistrophic reflectance at each site. The ratios proposed in this study

is able to identify the distinct shape with focus on the difference between forward, backward and nadir scattering. Here An, Da, Df stand for camera zenith angle equal to 0º, -70.5º, and 70.5º respectively.

$$\text{BandRatio1} = \frac{\rho An}{\frac{1}{2}(\rho Da + \rho Df)} \tag{6}$$

$$\text{BandRatio2} = \frac{\rho Df - \rho An}{\rho Da - \rho An} \tag{7}$$

4. RESULTS

4.1 DEM Generated from WorldView Stereo Image Pair

To ensure the consistent condition of the resulting DEM and have an adequately sized study area. Two sets of product that acquired by WorldView-1 satellite sensor with time disparity less than 2 hours on December 27, 2013 were used. The stereo image pairs were referenced to Radarsat Antarctic Mapping Project Digital Elevation Model Version 2 (RAMPv2_wgs84_200m.tif) with spatial resolution of 200 m and elevation relative to the WGS84 ellipsoid. The final DEM product and eleven study sites that used in the following study are listed in Table 1. Because of the presence of cloud, there are some regions with no valid elevations causing holes in the resulting DEM which were excluded from analysis.

Table 1 Surface type and coordinates of 11 study sites

SITE NUMBER	SURFACE TYPE	LATITUDE	LONGITUDE
1	Sea Ice	-77.68303103	165.9223516
2	Sea Ice	-77.73801679	165.8389805
3	Sea Ice	-77.77187272	166.0635656
4	Sea Ice	-77.71767917	164.8384062
5	Sea Ice	-77.66772316	164.4420813
6	Ice Shelf - Snow Typically	-77.83684324	165.8690605
7	Ice Shelf - Snow Typically	-77.87512575	165.8858435
8	Ice Shelf - Snow Free	-77.94628258	166.1086155
9	Ice Shelf - Snow Free	-78.0227833	166.1246517
10	Ice Shelf - Snow Free	-78.0324312	165.9251359
11	Glacier	-78.02752968	164.8274685

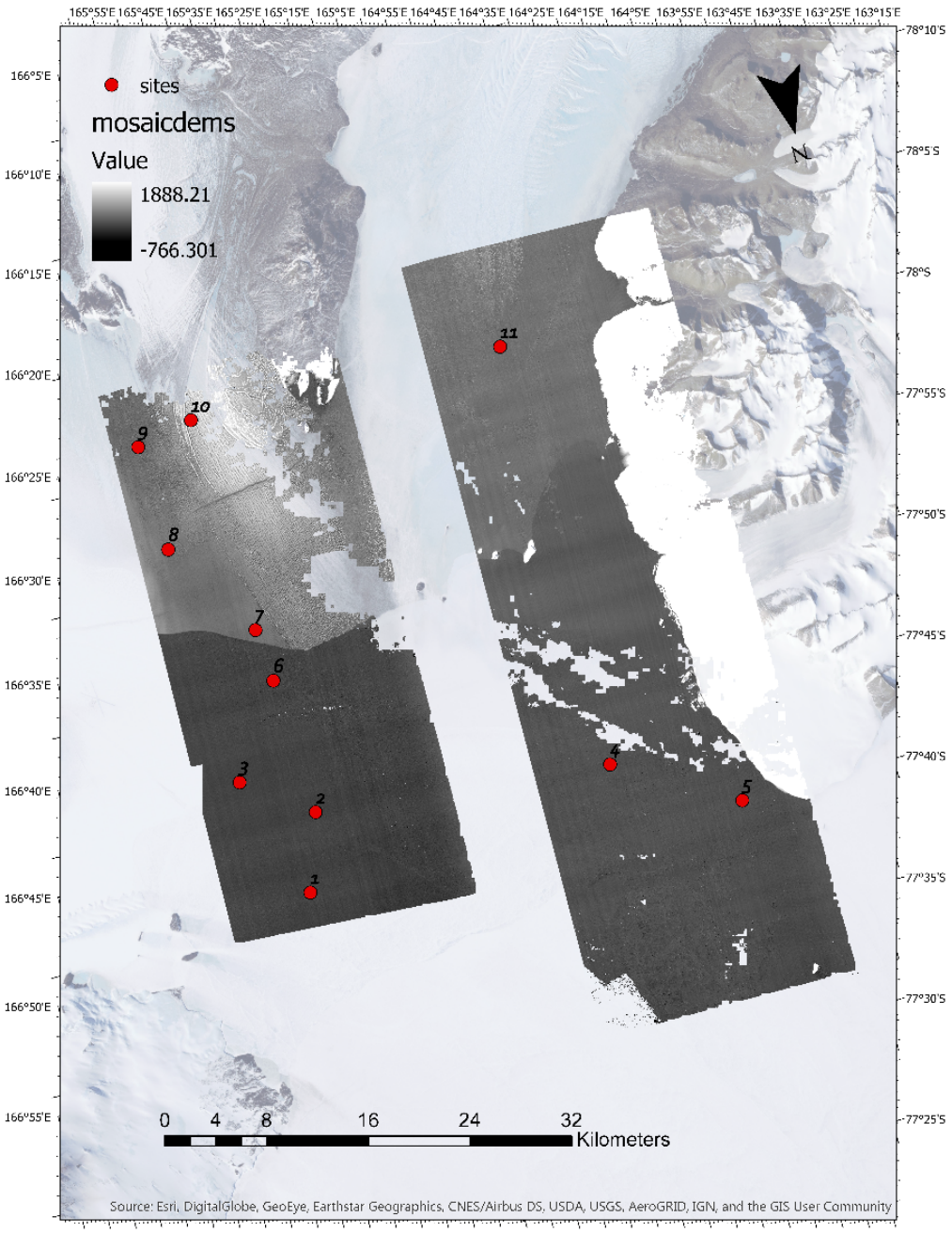

Figure 10 Final DEM generated from WorldView-1 stereo image pairs

4.2 DEM Elevation Accuracy

The DEM created using the Ames Stereo Pipeline was compared with near-

concurrent airborne LiDAR data acquired by the Airborne Topographic Mapper (ATM). From the original ATM LiDAR products, a DEM with 2 m resolution was generated.

Three transects over the ATM and Worldview 1 DEMs were selected for comparison and are indicated with different colors in figure 11. Elevations were extracted respectively from our generated DEM and the ATM LiDAR along the transects and the direction is same as the travel of airborne LiDAR. The first 500 pixels along each transect were selected and plotted against the distance from the start of the transect. The Root mean square error (RMSE) of first 500 pixels of DEM relative to LiDAR on transect 1, 2, 3 were 0.608, 0.751, and 0.610 m respectively. The comparison of elevation from the DEM generated from WorldView 1 and from ATM LiDAR are shown in figure 12. RMSE was computed as

$$RMSE = \sqrt{\frac{1}{n} * \sum_{i=1}^{n} (x' - x)^2} \quad (8)$$

where n is the number of samples, x' is the elevation value from DEM generated by stereo image pairs and x is the elevation converted from ATM LiDAR data. The visual inspections and low RMSE indicate that the quality of the WorldView 1 DEM as sufficient for investigating surface roughness variations across our study site.

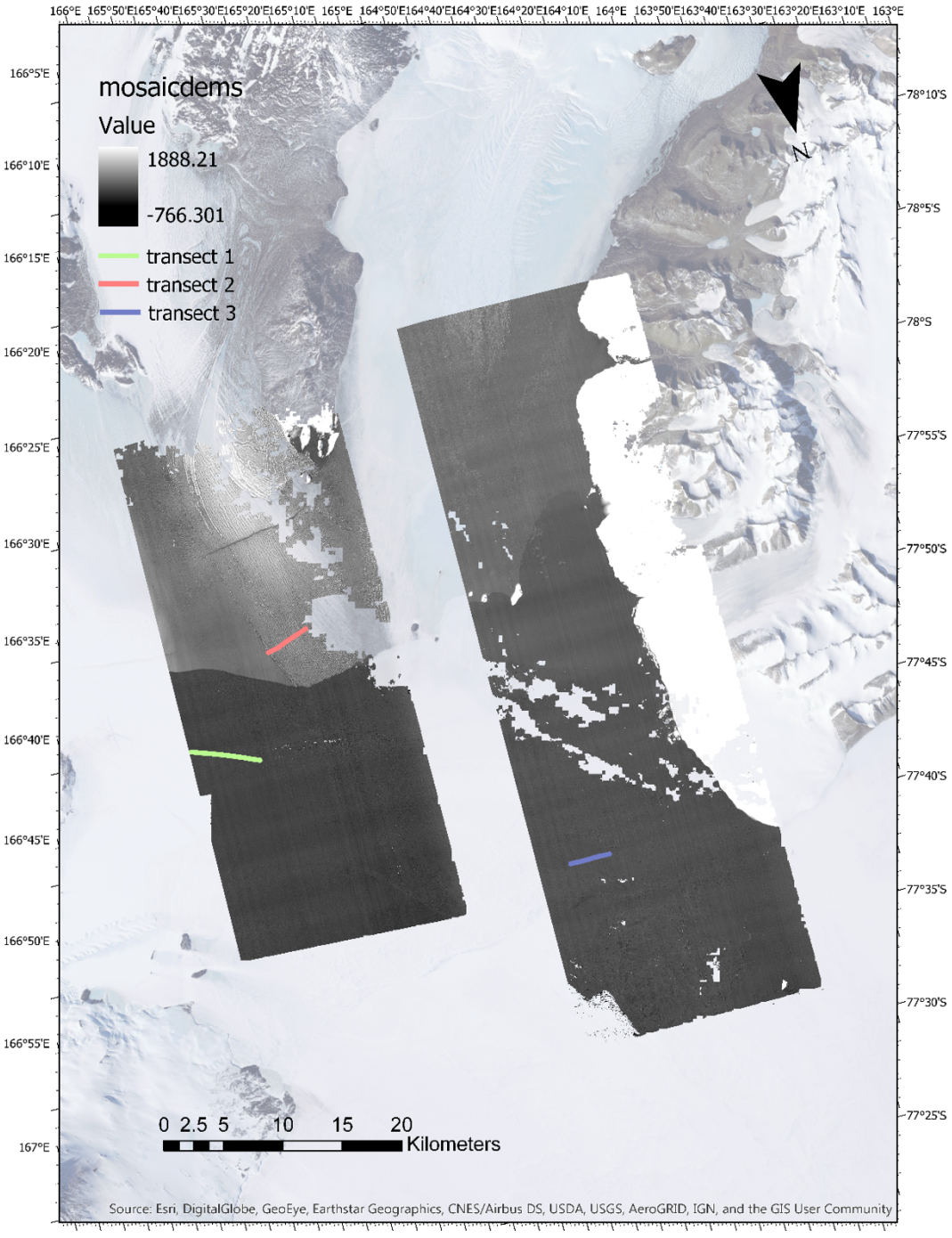

Figure 11 Location of three transects on track of airborne LiDAR over the DEM

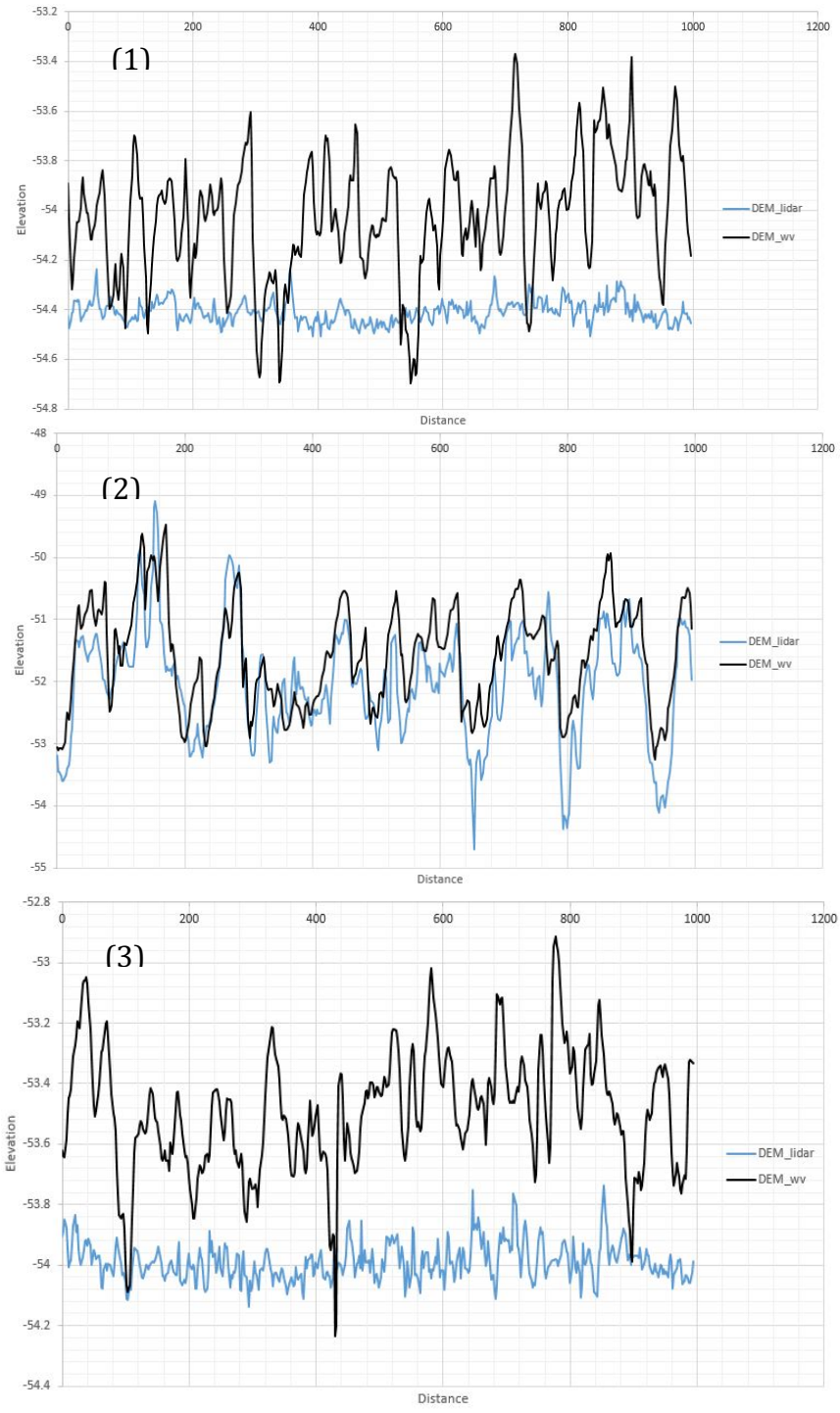

Figure 12 Comparison of absolute elevation value between DEM we generated from stereo satellite images and airborne LiDAR. Panel (1), (2), (3) are comparison based on first 100 pixels from transect 1, transect 2, and transect 3 respectively.

4.3 TRI Roughness Index

TRI surface roughness index was calculated on the DEM using various window size with both non-directional and directional kernels. Figure 13 shows the TRI index map when processing window size equals to 30 m and do not consider directionality. High elevations on the west side of the study area were excluded in the TRI computation because the emphasis of this study is small-scale surface roughness over relatively flat sea ice and McMurdo ice shelf. Figure 14 displays the comparison of four partial directional TRI maps which measure the elevation differences in four different directions: north-south, east-west, northwest-southeast, and northeast-southwest compared to the center pixel.

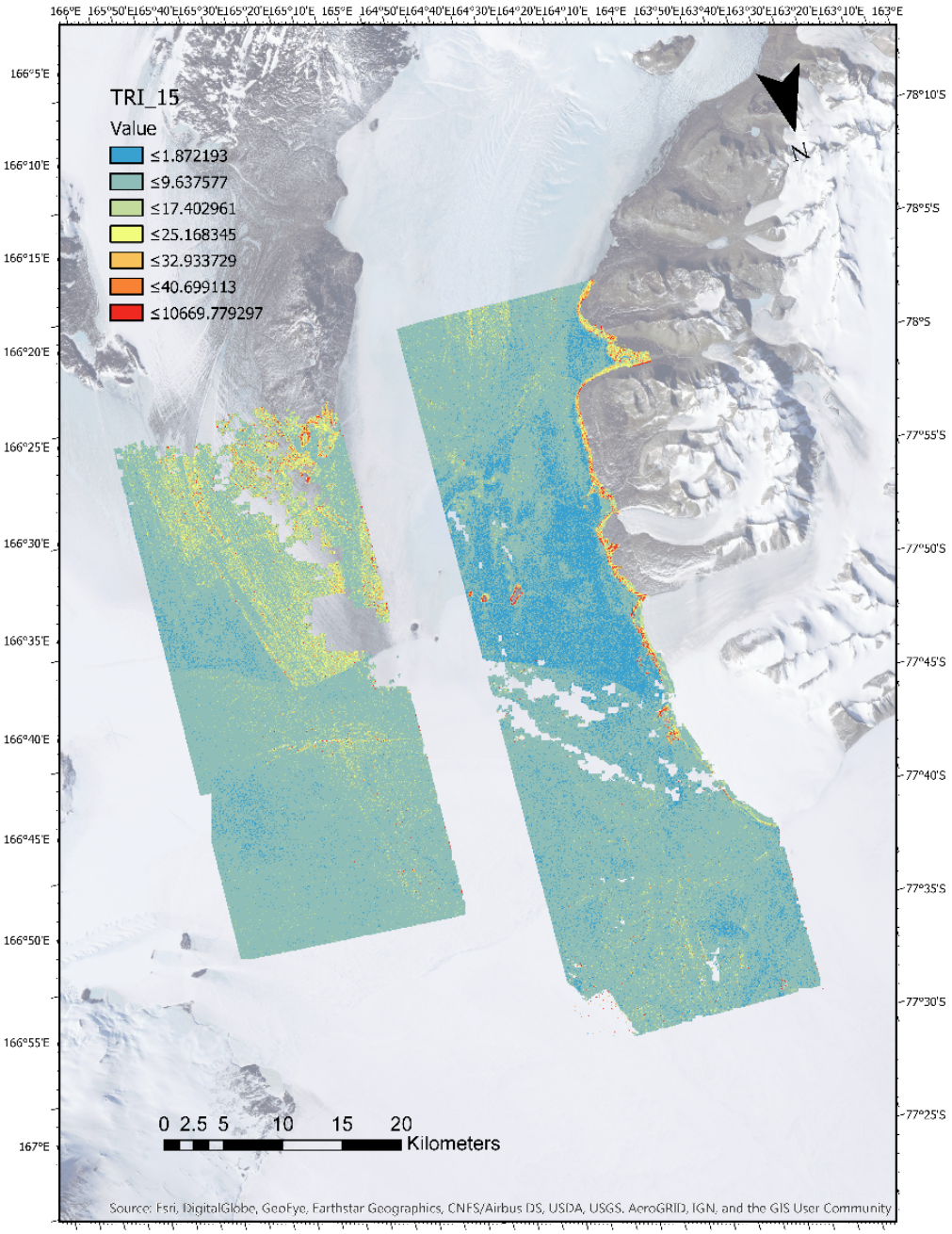

Figure 13 Terrain Ruggedness Index when processing window size is 30 m

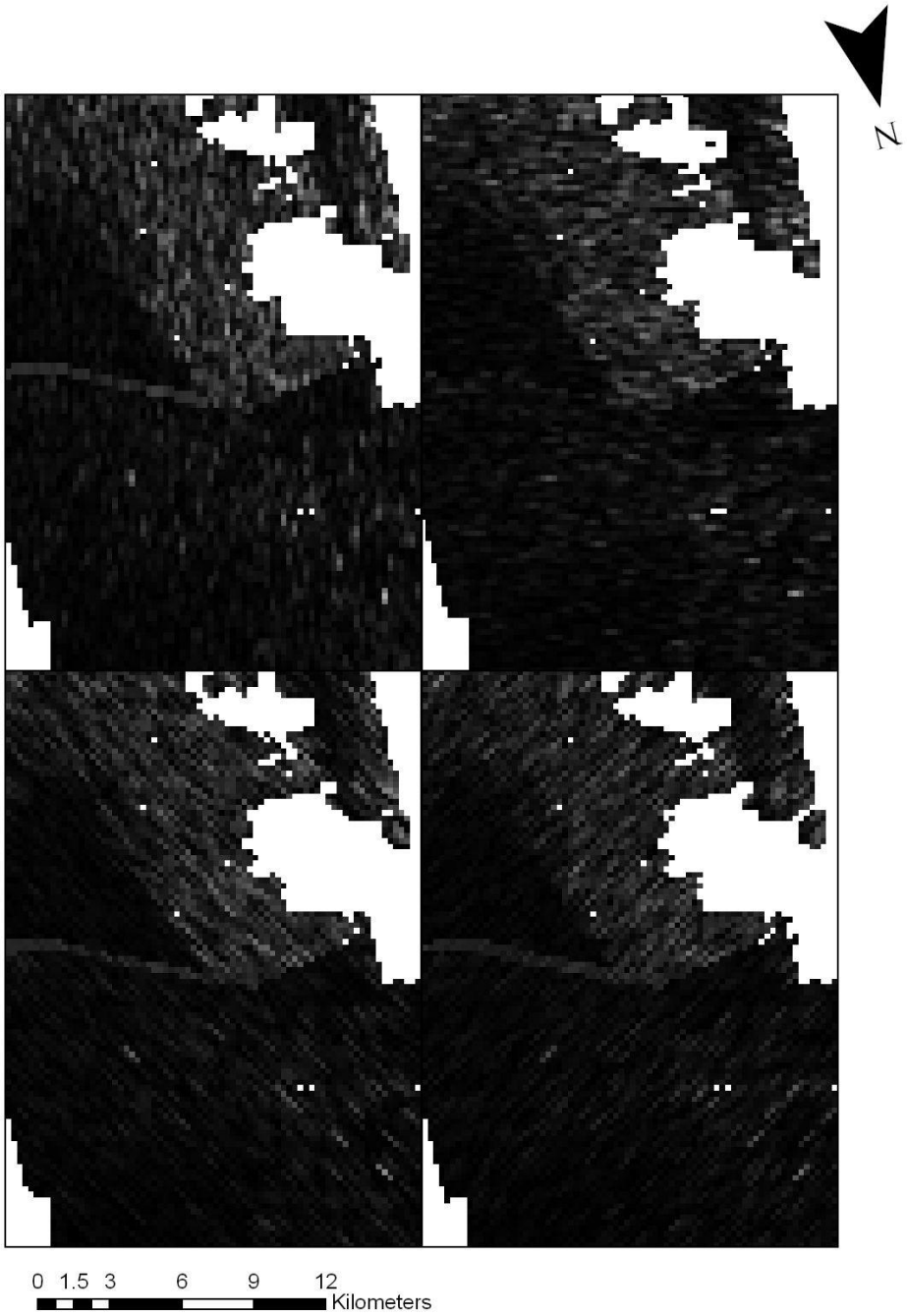

Figure 14 Partial Terrain Ruggedness Index with 234 m cell size in four directions. Upper left: north-south, upper right: east-west, lower left: northwest-southeast, lower right: northeast-southwest

The changes of the TRI with the increasing window size in selected sites are

shown in the Figure 15. Since the variation of TRI becomes more significant at larger window sizes, TRI variations as a function of window size were also investigated as a function of the natural logarithm of window size as illustrated in Figure 16. An exponential function was fit to the TRI with increasing window size using a one parameter function with an intercept at (0, 0) to keep the function as parsimonious a s possible:

$$y = \exp(k * x) - 1 \quad (9)$$

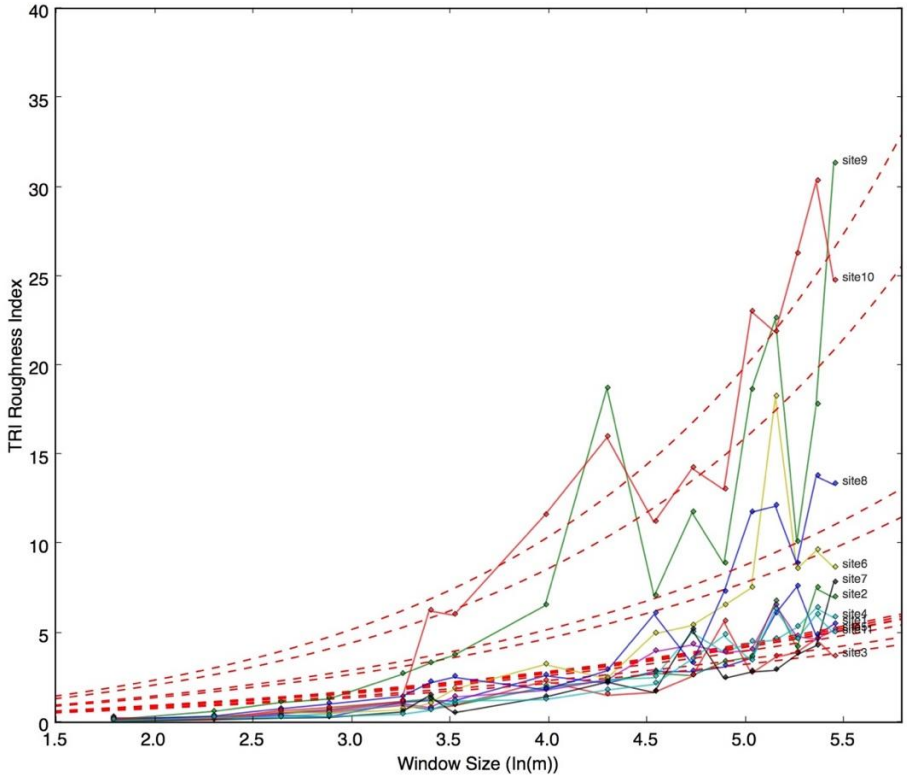

Figure 15 Un-normalized TRI roughness change with calculation window size

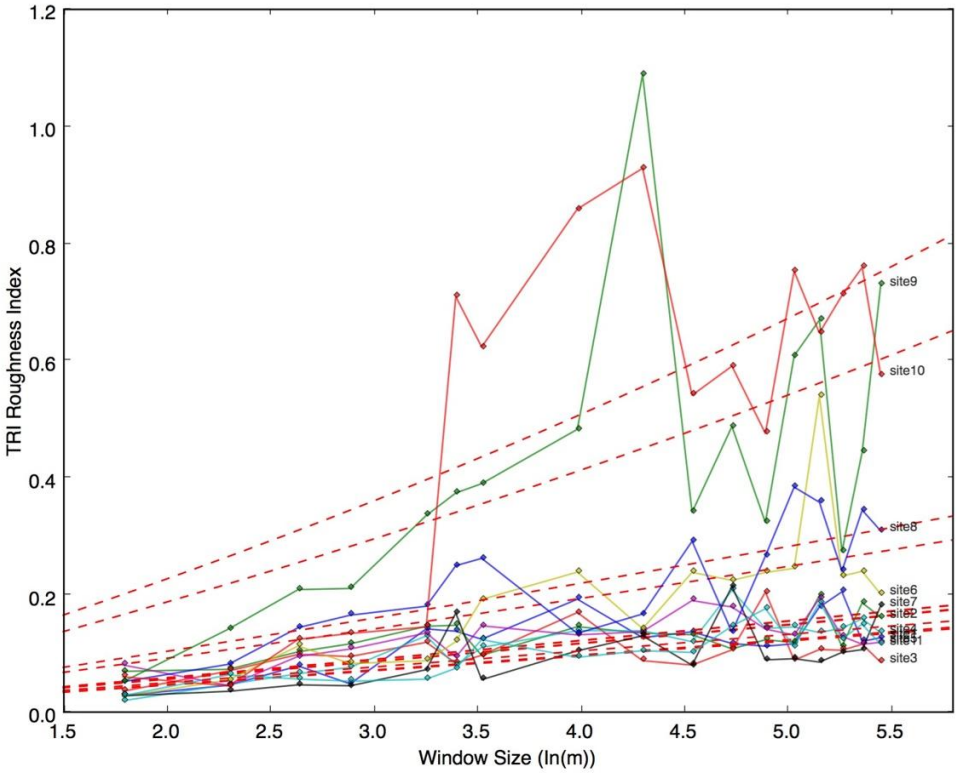

Figure 16 Normalized TRI roughness change with calculation window size

It is clear that the k in function 9 parameter captures differences in how TRI changes with increasing pixel size which is in turn related to surface type (Table 1). The k parameter in equation 9 for each site from site 1 to site 11 are 0.33112469, 0.33778873, 0.29007223, 0.33438777, 0.33021749, 0.43583286, 0.30300383, 0.45657646, 0.56558668, 0.60790733, and 0.32215089.

One thing need to be motioned here is the computation strategy difference of non-directional TRI and directional TRI. When calculating the non-directional TRI surface toughness index, the resulting TRI map has the spatial resolution same as the calculating window size since all the pixels inside the moving window produce one shared value. When it comes to directional TRI, original DEM was resampled to the

desired cell size. As the moving window shifted from left to right and top to bottom pixel by pixel, TRI map was generated with the same spatial resolution as resampled DEM for the calculated TRI was assigned to center pixel only in the moving window.

4.4 MRPV BRDF Model

The mRPV model was built to describe the anisotropic scattering of target sites. Three parameters (r_0, k, b) explain the anisotropy of target required by mRPV model are obtained from MISR Level-2 Land Surface product. Another important parameter, solar zenith angle is acquired from MISR Level-1B2 Geometric Parameters product. MRPV model is able to approximate the Bidirectional Reflectance Factor (BRF) for any given viewing zenith angle and azimuth angle relative to the sun. Figure 17, 18, and 19 illustrate the BRF value at site 6, 9, and 10 simulated by mRPV model in blue, green, red, and NIR band respectively.

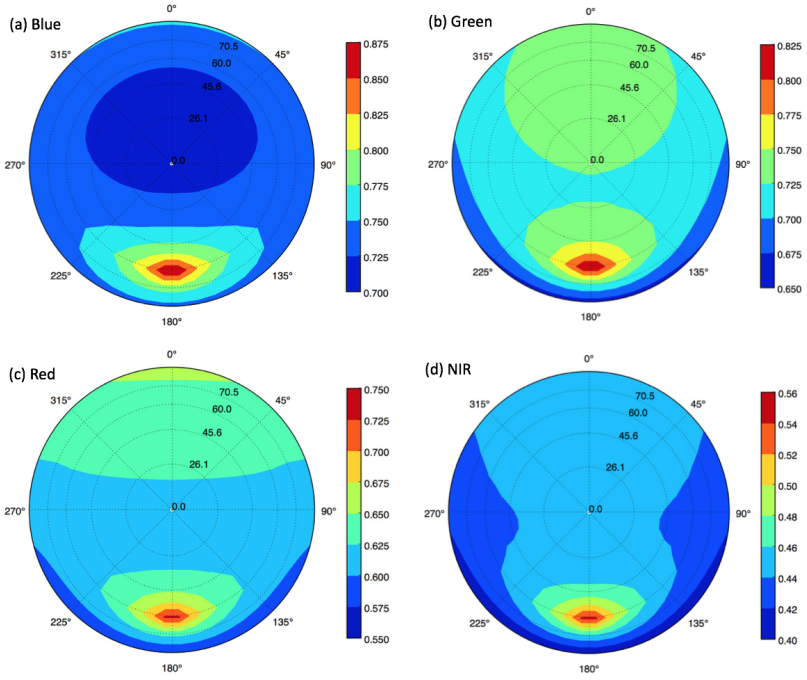

Figure 17 MRPV model for site 6 in MISR blue band (a), green band (b), red band (c), NIR band (d)

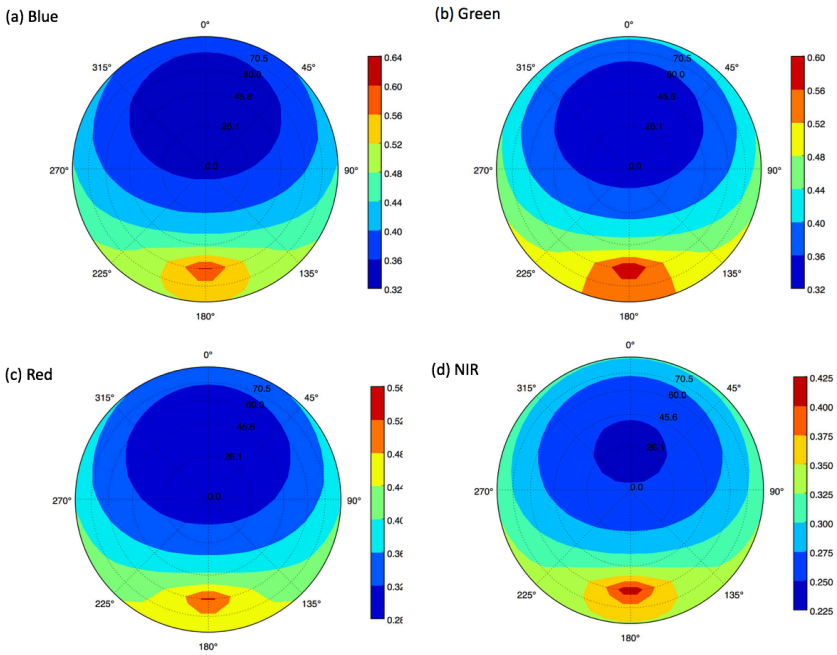

Figure 18 MRPV model for site 9 in MISR blue band (a), green band (b), red band (c), NIR band (d)

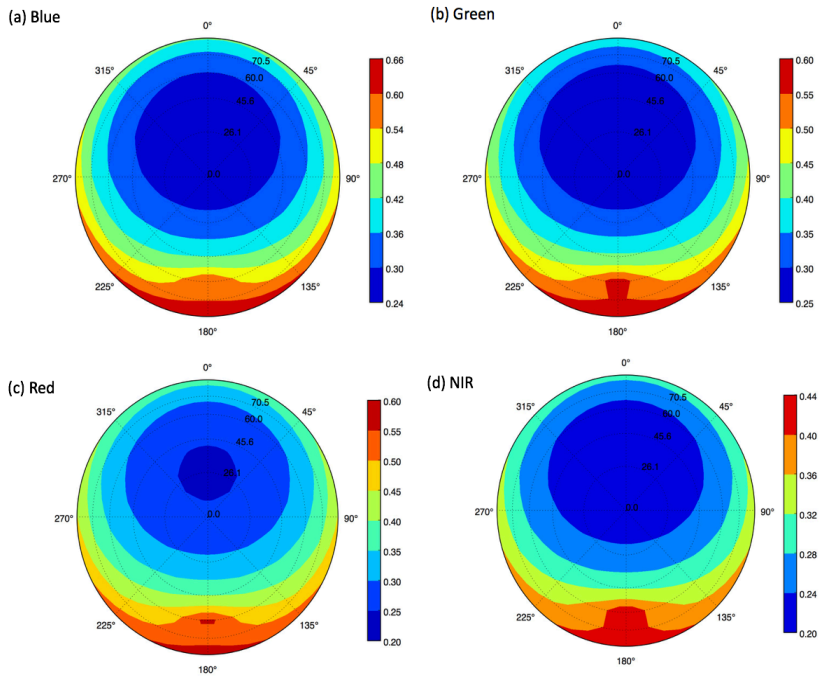

Figure 19 MRPV model for site 10 in MISR blue band (a), green band (b), red band (c), NIR band (d)

4.5 MISR NDAI and Other Angular Ratios

In order to minimize the disturbance of atmosphere on surface BRFs, a cloud free condition is required. MISR images from path 59 was selected for its least cloud percentage of all MISR images studied. All the examinations on angular distribution of surface scattering over study area were performed on images from path 59, block 154 and orbit 074640 acquired on December 29, 2013.

Figure 20 indicates the top of atmosphere radiance in nine different viewing angles over eleven sites with various surface conditions in four bands. The average solar zenith angle of the whole entire is about 61.3º. The definition of relative azimuth angle in MISR product is the view azimuth angle with respect to the Sun position in reference

to ellipsoid system and value is 0º when the Sun is behind viewing camera. It is easy to infer from the ancillary data that forward cameras (positive zenith angles in the figure 3) captured backward scattering and afterward cameras indicate forward scattering at this specific illumination and observation geometry.

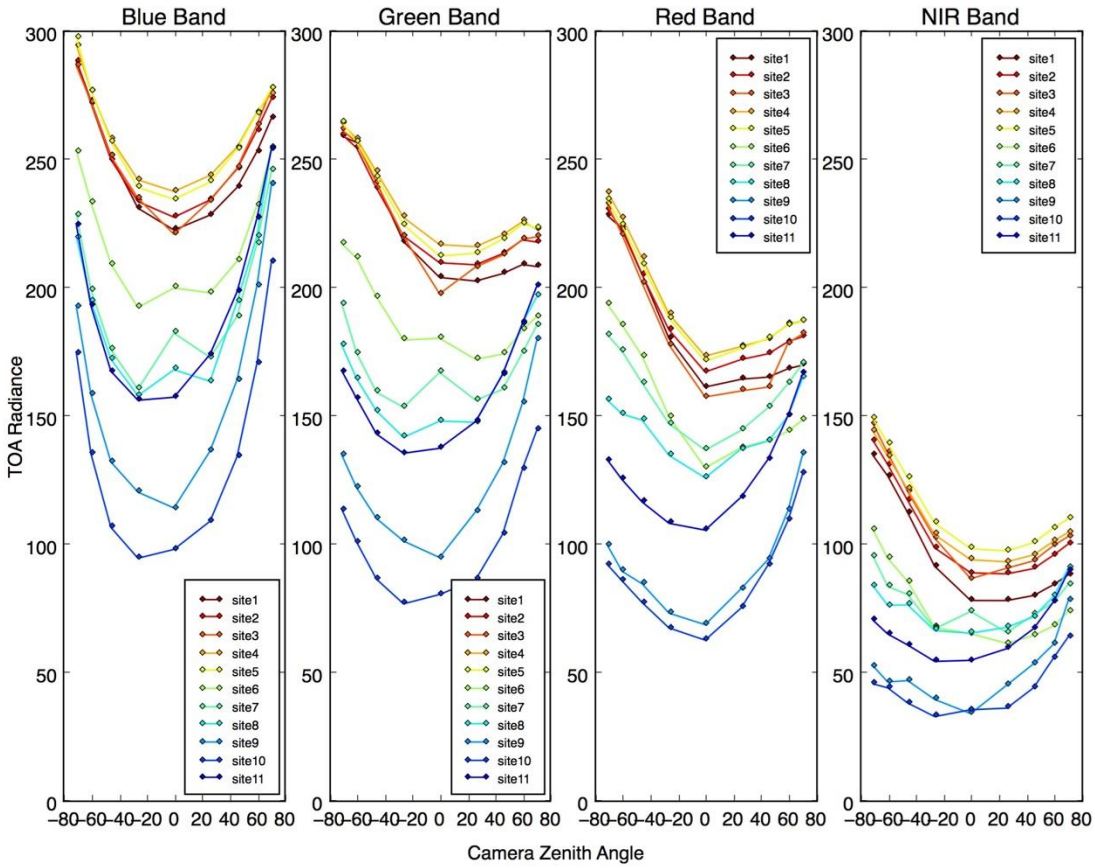

Figure 20 Radiance value in various viewing angles: 0 º (An), 26.1 º(A), 45.6 º(B), 60 º(C), and 70.5 º(D) in forward (f) and afterward (a) directions.

In order to have a better understanding of anisotropic scattering pattern in study area, we compared radiance in An and Da angle and calculated correlation in Figure 21. If the study site is an ideal isotropic scattering object, the radiance value in An and Da should be identical. Again, the MISR red band was selected since it has highest spatial

resolution. The points in the scatter plot are obtained from a 7*7 window surrounding the selected study pixels.

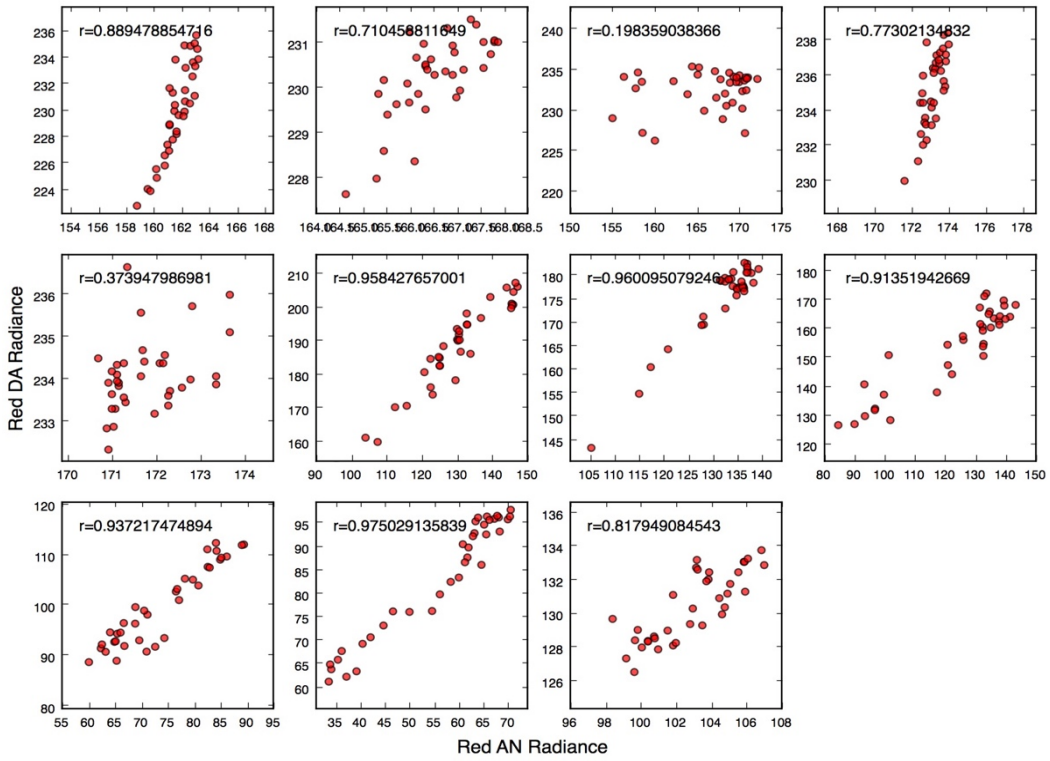

Figure 21 Scatter plot illustrating correlations between MISR An and Da cameras radiance value in 11 sites. Plots from top to bottom and left to right represent site 1 to site 11.

Figure 22 visualizes the radiance change with surface roughness index by plotting the two radiance ratios proposed in this study against k parameter value of the fitted function 9.

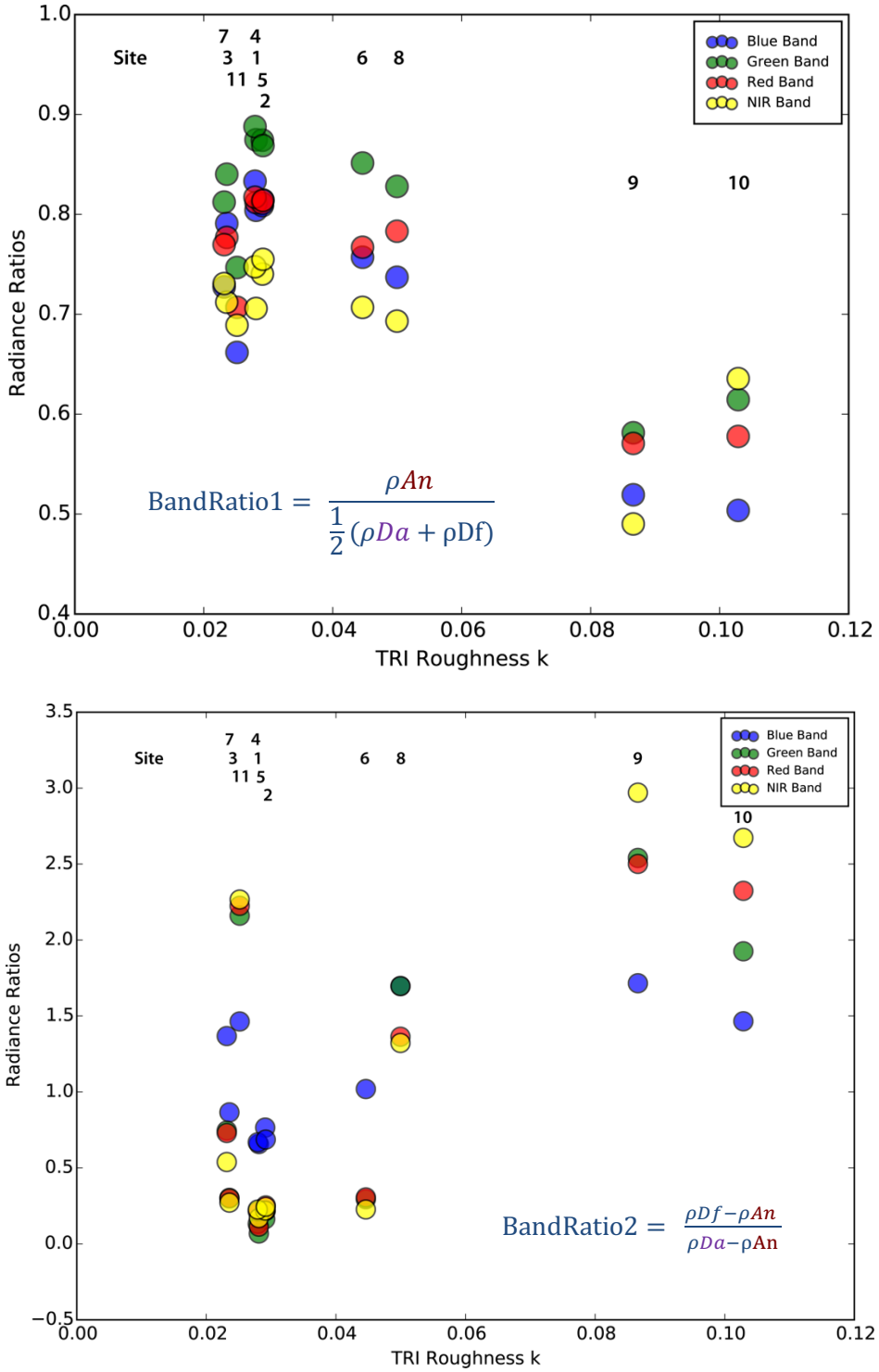

Figure 12 Scatter plots of TRI roughness fitted function k parameter against band ratio 1 (upper) and 2 (lower)

5. DISCUSSION

5.1 DEM Extraction from WorldView-1 Stereo Image Pair

This study demonstrated the potential of very high spatial resolution WorldView-1 stereo satellite images in mapping topographic roughness at large scale in a remote polar area across sea ice and ice shelf surfaces. The resulting DEM processed form Ames Stereo Pipeline has the same 2 me grid size as the WorldView-1. The DEM product in this study has the highest spatial resolution in the study area comparing with other available elevation data sources. Despite the advantage of stereo image pairs in large scale mapping application, the existence of cloud and ice surface lacking of large scale features limit the performance of generating DEM.

Due to the lack of ground control points (GCPs), preliminary DEM product obtained from *stereo* was aligned to a terrain converted from ATM LiDAR data. Although LiDAR has a centimeter level of error in vertically, it is better than the uncorrected DEM from ASP program with meter scale vertical error.

5.2 DEM Accuracy Assessment

The ATM LiDAR data was divided in two groups. One set of LiDAR was used as control data in the process of DEM generation, we compared another set of LiDAR data for DEM accuracy elevation. LiDAR data are acquired over the same time period as the acquisition of WorldView satellite images. The Root Mean Square Error (RMSE) for the three transects we selected along the LiDAR data footprints are quite low (0.608, 0.751, and 0.610 meters, respectively). These low RMSE values demonstrated a great improvement on the vertical accuracy after the DEM registration. Transect 1 and transect

3 are over sea ice and have a relatively smooth surfaces, while transect 2 is over the ice shelf with snow which is a rougher surface. It is easy to notice by visual comparison that the track crossing a relatively smooth portion of ice (track 1 and track 3) shows a weaker correlation in elevations between the Worldview 1and LiDAR DEMs but a relatively small difference in less difference in absolute elevations. The LiDAR data in transect 2 displays a larger variation in elevation and the DEM generated from WorldView-1 stereo images has a stronger correlation with LiDAR elevations. However, the absolute elevation difference between DEM and LiDAR is much greater in transect 3 than the other two transects as measured by RMSE. The difference in performance over smooth and rough surface can be explained by how ASP generating topography. The correlation step is performed in a two-step pyramid algorithm in ASP. The low resolution version of the input stereo images is created first and the disparity map is found. Then the disparity map is refined by increasing the input images to higher resolution (ASP book). This approach works better for rocky terrain but may fail for snowy surface, which only has features with small-scale sastrugi or ridges shaped by wind. Thus small structures may disappear at low resolution and the information may get lost in the first step of correlation algorithm. So the ability of generating topography at smooth surface is not as good as the surfaces with greater relief. However, it is important to note that the local roughness features on transect 3 were only on the order of 2 meters, so while the WorldView DEM appears to differ from the LiDAR DEM for very smooth surfaces with local roughness of approximately a meter, it appears to do well in capturing variations in surface roughness of more than a meter

5.3 TRI Roughness Map Evaluation

The resulting DEM created by the Ames Stereo Pipeline is the only input for calculating Terrain Ruggedness Index (TRI). TRI is an index widely used in quantifying landscape roughness by computing the average change in elevation between a center cell and its surrounding cells within the moving window. By dividing the average change by the calculating window size, the value of index is normalized and the magnitude difference caused by number of pixels in calculation is eliminated.

It is evident in Figure 15 that TRI values do not change significantly when the window size is very small (less than 20 m) on these sea ice and ice shelf surfaces. As the window size increase to larger than 20 m, TRI values experience a great increase at sites 9 and 10 which are located on ice shelves with very rough surfaces. It is possible to infer that the spatial scale of the peak roughness structure is around 20 m at site 9 and 55 m at site 10. Combined with the WorldView-1 high resolution satellite images, it is easy to discover that ice shelves have multi-year ice without snow are rougher than the ice shelves covered with snow. And the McMurdo Ice shelf is in general are rougher than sea ice. Older sea ice is rougher than first year sea ice which are closer to the open water in our study area.

5.4 MRPV BRDF Model

BRDF angular distributions simulated with mRPV model are illustrated in hemispherical space at site 6, 9, and 10 in Figure 17, 18, and 19. Overall, snow and ice has very high BRF because they are highly reflective at visible wavelength. In site 6, BRF values are greater than 0.55 in visible bands except the NIR band with lowest BRF

value at 0.4. As we can see from three BRF model figures, BRF generally decreases with the increase of wavelength from blue, green, red, to NIR which is in accordance with spectral signature of snow and ice. The model is simulated with solar zenith angle value to be 60.605º, 60.667 º, 60.742 º at the time of MISR data acquisition in site 6, 9, and 10 respectively. A relative azimuth of 180º and viewing zenith angle of 60º has the highest BRF which indicates the domination of forward scattering over study area. Minimum reflectance occurs around the nadir zenith angle and the distribution shape is similar to bowl which is in accordance with MISR 9 cameras radiance in figure 20. The center of low BRF values moves from nadir to backward direction from blue band to NIR band. At the same time, a new region of low BRF values occurs at the forward direction when view zenith angle is extremely large (greater than 75º). As the surface roughens from 6 to 9 and finally 10, the forward scattering peak is weakened and the geometry of BRDF model becomes more symmetrical which means the reflectance is more isotropic.

5.5 Angular Scattering Signature of Antarctica Snow and Ice

BRDF model provides information about how surface reflect illumination and energy in a hemispherical space and continuous BRF values are accessible in all directions. However, the BRF calculated from the model are estimated values under ideal environmental conditions. Thanks to the angular information provided by MISR multi-angle cameras, actual reflectance captured by satellite sensors are able to be used in analysis. Examination of surface roughness and its influence on angular scattering pattern was performed on 11 sites in this study.

When we plot the radiance values from Da, Ca, Ba, Aa, An, Af, Bf, Cf, Df

cameras against viewing zenith angle as shown in Figure 20, lower radiances are found near nadir (An) and higher values at the extreme forward and aft view angles (Af, Df). Extreme angle reveals a bowl-shape scattering pattern caused by higher radiances from the forward and aft cameras compared to the nadir views. With increasing wavelength, both the absolute radiance and depth of bowl shape decrease.

The change of shape across camera view angles with increasing wavelength again evidences an increase in forward scattering with wavelength expected for snow and ice. Sites 1 to 5 have higher value in aft camera which indicates forward scattering because they are relatively smooth and forward scattering prevail in the scattering signature. For site 6-8, the forward scattering and backward scattering are more similar. For sites 9 -11 forward cameras and backward scattering dominate from these rougher sites.

Besides the comparison of radiance value in nine different zenith angles, we have also examined the correlation between nadir and off-nadir bands for each site. Under an ideal circumstance where scattering of solar energy are exactly the same in all direction, radiance value in An and Da bands should be the same for every single pixel. Sites 6-10 are highly correlated in the red band An and red band Da with Pearson correlation coefficient greater than 0.9. Sites 3 and 4 exhibit the lowest correlation between scattering in An and Da angles.

6. CONCLUSION AND FUTURE WORK

This research demonstrated the ability of high spatial resolution Worldview 1 stereo images pairs to produce DEMs that capture spatial variability on low relief sea ice and ice shelf surfaces in the Ross Sea region. These DEMs compare favorably to LiDAR-derived profiles acquired near the same time. As one of the main methods people used to collect elevation data, satellite imagery stereo pairs should be highly regarded for their convenience in data acquisition and high spatial resolution at large scale.

This study also investigated the scattering pattern of snow and ice surfaces on sea ice in McMurdo Sound and adjacent portions of the McMurdo Ice Shelf by simulating the Bidirectionall reflectance factor (BRF) with the mRPV semi-empirical model. Three independent parameters (r_0, k, b) are provided by MISR surface product. Along with the information of sun position, we are able to retrieve the reflectance under any viewing geometry. To test the reliability of mRPV model, we take advantage of multi-angle observing ability of MISR sensors and evaluated the anisotropic scattering over study area by several normalized index of difference between backward-scattered radiance and forward-scattered radiance. We demonstrated that surface condition has influence on reflectance pattern on snow and ice in Antarctica where satellite pixels are pure and are not contaminated by other features. A smooth snow surface has a reflectance peak in the forward direction, while rough surface structures weaken the forward scattering characteristics of snow and ice and has further impact on pixel values on satellite

images.

Future work will focus on quantify the influence of surface roughness on the BRDF model and improve the model to have more accurate simulation on the scattering signature of snow and ice. None of the BRDF model currently used by researches incorporates surface roughness. If the impact of small surface structures are considered in the model, the estimation accuracy of ground object characteristic with quantitative remote sensing approach will be significantly improved.

REFERENCES

Braithwaite, R. J., and O. B. Olesen. 1993. Seasonal-variation of ice ablation at the margin of the Greenland ice-sheet and its sensitivity to climate-change, Qumanarssup-Sermia west Greenland. *Journal of Glaciology* 39 (132):267-274.

Buyuksalih, G., G. Kocak, M. Oruc, H. Akcin, and K. Jacobsen. 2004. Accuracy analysis, DEM generation and validation using Russian TK-350 stereo-images. *Photogrammetric Record* 19 (107):200-218.

Diner, D., Martonchik, J., Borel, C., Gerstl, S., Gordon, H., Knyazikhin, Y., Myneni, R. Pinty, B. & Verstraete, M. 1999. MISR: Level 2 Surface Retrieval Algorithm Theoretical Basis (Revision D). Jet Propulsion Laboratory, California Institute of Technology.

Dozier, J., and T. H. Painter. 2004. Multispectral and hyperspectral remote sensing of alpine snow properties. *Annual Review of Earth and Planetary Sciences* 32:465-494.

Gobron, N., B. Pinty, M. M. Verstraete, J. L. Widlowski, and D. J. Diner. 2002. Uniqueness of multiangular measurements - Part II: Joint retrieval of vegetation structure and photosynthetic activity from MISR. *Ieee Transactions on Geoscience and Remote Sensing* 40 (7):1574-1592.

Herzfeld, U. C. 1999. Geostatistical interpolation and classification of remote sensing data from ice surfaces. *International Journal of Remote Sensing* 20 (2):307-327.

Herzfeld, U. C., H. Mayer, W. Feller, and M. Mimler. 2000. Geostatistical analysis of

glacier-roughness data. In *Annals of Glaciology, Vol 30, 2000*, ed. K. Hutter, 235-242. Cambridge: Int Glaciological Soc.

Hong, S. 2010. Detection of small-scale roughness and refractive index of sea ice in passive satellite microwave remote sensing. *Remote Sensing of Environment* 114 (5):1136-1140.

Johnson, G. C. 2008. Quantifying Antarctic bottom water and north Atlantic deep water volumes. *Journal of Geophysical Research-Oceans* 113 (C5):13.

Kaufman, Y. J., N. Gobron, B. Pinty, J. L. Widlowski, and M. M. Verstraete. 2002. Relationship between surface reflectance in the visible and mid-IR used in MODIS aerosol algorithm - theory. *Geophysical Research Letters* 29 (23):4.

Kuchiki, K., T. Aoki, M. Niwano, H. Motoyoshi, and H. Iwabuchi. 2011. Effect of sastrugi on snow bidirectional reflectance and its application to MODIS data. *Journal of Geophysical Research-Atmospheres* 116:15.

Kuhn, M. 1985. Bidirectional reflectance of polar and alpine snow surfaces. *Annals of Glaciology-Series* 6:164-167.

Landy, J. C., D. Isleifson, A. S. Komarov, and D. G. Barber. 2015. Parameterization of centimeter-scale sea ice surface roughness using terrestrial LiDAR. *Ieee Transactions on Geoscience and Remote Sensing* 53 (3):1271-1286.

Leroux, C., and M. Fily. 1998. Modeling the effect of sastrugi on snow reflectance. *Journal of Geophysical Research-Planets* 103 (E11):25779-25788.

Li, X. W., and A. H. Strahler. 1992. Geometric-optical bidirectional reflectance modeling of the discrete crown vegetation canopy – effect of crown shape and

mutual shadowing. *Ieee Transactions on Geoscience and Remote Sensing* 30 (2):276-292.

Lyapustin, A., M. Tedesco, Y. J. Wang, T. Aoki, M. Hori, and A. Kokhanovsky. 2009. Retrieval of snow grain size over Greenland from MODIS. *Remote Sensing of Environment* 113 (9):1976-1987.

Martonchik, J. V., B. Pinty, and M. M. Verstraete. 2002. Note on "an improved model of surface BRDF-atmospheric coupled radiation". *Ieee Transactions on Geoscience and Remote Sensing* 40 (7):1637-1639.

Noh, M. J., and I. M. Howat. 2015. Automated stereo-photogrammetric DEM generation at high latitudes: surface extraction with TIN-based search-space minimization (SETSM) validation and demonstration over glaciated regions. *Giscience & Remote Sensing* 52 (2):198-217.

Noh, M. J., and I. M. Howat. 2017. The surface extraction from TIN based search-space Minimization (SETSM) algorithm. *Isprs Journal of Photogrammetry and Remote Sensing* 129:55-76.

Nolin, A. W. 2004. Towards retrieval of forest cover density over snow from the Multi-angle Imaging SpectroRadiometer (MISR). *Hydrological Processes* 18 (18):3623-3636.

Nolin, A. W., F. M. Fetterer, and T. A. Scambos. 2002. Surface roughness characterizations of sea ice and ice sheets: Case studies with MISR data. *Ieee Transactions on Geoscience and Remote Sensing* 40 (7):1605-1615.

Nolin, A. W., and M. C. Payne. 2007. Classification of glacier zones in western

Greenland using albedo and surface roughness from the Multi-angle Imaging SpectroRadiometer (MISR). *Remote Sensing of Environment* 107 (1-2):264-275.

Painter, T. H., K. Rittger, C. McKenzie, P. Slaughter, R. E. Davis, and J. Dozier. 2009. Retrieval of subpixel snow covered area, grain size, and albedo from MODIS. *Remote Sensing of Environment* 113 (4):868-879.

Rahman, H., M. M. Verstraete, and B. Pinty. 1993. Coupled surface-atmosphere reflectance (CSAR) model description and inversion on synthetic data. *Journal of Geophysical Research-Atmospheres* 98 (D11):20779-20789.

Rivas, M. B., J. A. Maslanik, J. G. Sonntag, and P. Axelrad. 2006. Sea ice roughness from airborne LIDAR profiles. *Ieee Transactions on Geoscience and Remote Sensing* 44 (11):3032-3037.

Roy, D. P., H. K. Zhang, J. Ju, J. L. Gomez-Dans, P. E. Lewis, C. B. Schaaf, Q. Sun, J. Li, H. Huang, and V. Kovalskyy. 2016. A general method to normalize Landsat reflectance data to nadir BRDF adjusted reflectance. *Remote Sensing of Environment* 176:255-271.

Scambos, T. A., T. M. Haran, M. A. Fahnestock, T. H. Painter, and J. Bohlander. 2007. MODIS-based mosaic of Antarctica (MOA) data sets: continent-wide surface morphology and snow grain size. *Remote Sensing of Environment* 111 (2-3):242-257.

Stamnes, K., W. Li, H. Eide, T. Aoki, M. Hori, and R. Storvold. 2007. ADEOS-II/GLI snow/ice products - Part I: Scientific basis. *Remote Sensing of Environment* 111 (2-3):258-273.

Stroeve, J., J. E. Box, F. Gao, S. L. Liang, A. Nolin, and C. Schaaf. 2005. Accuracy assessment of the MODIS 16-day albedo product for snow: comparisons with Greenland in situ measurements. *Remote Sensing of Environment* 94 (1):46-60.

Stroeve, J. C., T. Markus, J. A. Maslanik, D. J. Cavalieri, A. J. Gasiewski, J. E. Heinrichs, J. Holmgren, D. K. Perovich, and M. Sturm. 2006. Impact of surface roughness on AMSR-E sea ice products. *Ieee Transactions on Geoscience and Remote Sensing* 44 (11):3103-3117.

Stroeve, J. C., and A. W. Nolin. 2002. New methods to infer snow albedo from the MISR instrument with applications to the Greenland ice sheet. *Ieee Transactions on Geoscience and Remote Sensing* 40 (7):1616-1625.

Wanner, W., X. Li, and A. H. Strahler. 1995. On the derivation of the kernels for kernel-driven models of bidirectional reflectance. *Journal of Geophysical Research-Atmospheres* 100 (D10):21077-21089.

Warren, S. G., R. E. Brandt, and P. O. Hinton. 1998. Effect of surface roughness on bidirectional reflectance of Antarctic snow. *Journal of Geophysical Research-Planets* 103 (E11):25789-25807.

Wiscombe, W. J., and S. G. Warren. 1980. A model for the spectral albedo of snow .1. pure snow. *Journal of the Atmospheric Sciences* 37 (12):2712-2733.

Zhou, X., and S. Li. 2003. Comparison between in situ and MODIS-derived spectral reflectances of snow and sea ice in the Amundsen Sea, Antarctica. *International Journal of Remote Sensing* 24 (24):5011-5032.

Zhuravleva, T. B., and A. A. Kokhanovsky. 2011. Influence of surface roughness on the

reflective properties of snow. *Journal of Quantitative Spectroscopy & Radiative Transfer* 112 (8):1353-1368.